Supplementary Information (SI) for Journal of Materials Chemistry A.
This journal is © The Royal Society of Chemistry 2026

Supporting information for

Covalent Functionalization of Polyhydroxyurethanes with Fluorescent Groups for Colorless Luminescent Solar Concentrators

Sergei V. Zubkevich†[a], Gaia Roberta Ragno†[b], Elisavet Tatsi†[b], Chiara Botta[c], Vincent Berthé[a], Laura Puchot[a], Stefano Turri[b], Daniel F. Schmidt*[a], Alexander S. Shaplov*[a] and Gianmarco Griffini*[b]

[a] Sergei V. Zubkevich, Vincent Berthe, Laura Puchot, Daniel F. Schmidt, Alexander S. Shaplov
Luxembourg Institute of Science and Technology (LIST), Functional Polymeric and Particulate Materials Unit,
5 Avenue des Hauts-Fourneaux, L-4362 Esch-sur-Alzette, Luxembourg
E-mail: A.S.: alexander.shaplov@list.lu; D.S.: daniel.schmidt@list.lu.

[b] Gaia Roberta Ragno, Elisavet Tatsi, Stefano Turri, Gianmarco Griffini
Department of Chemistry, Materials and Chemical Engineering "Giulio Natta"
Politecnico di Milano
Piazza Leonardo da Vinci 32, Milano 20133, Italy
E-mail: gianmarco.griffini@polimi.it

[c] Chiara Botta
Institute of Sciences and Chemical Technologies "Giulio Natta" (SCITEC) of CNR
Via A. Corti 12, 20133 Milano, Italy

Table of Contents

I. Materials

***Reagents**: meso*-erythritol (>99%, TCI Chemicals), diphenyl carbonate (99%, Sigma-Aldrich), (4-formylphenyl)boronic acid (98%, BLD Pharm), 2-bromofluorene (97 %, BLD Pharm), 4-hydroxybenzaldehyde (98%, BLD Pharm), 1,2-dibromoethane (99%, ABCR), 7-hydroxy-2H-chromen-2-one (7-Hydroxycoumarin, Umbelliferone >98%, TCI Europe), tetrakis(triphenylphosphine)palladium (0) (99%, Sigma-Aldrich), p-toluenesulfonic acid monohydrate (≥98%, Carl Roth), phosphorous pentoxide ((immobilized on silica, with indicator, Sicapent®, Sigma-Aldrich), lithium bis(trifluoromethanesulfonyl)imide (LiTFSI, 99.9 %, Solvionic), sodium carbonate (>99%, TCI Europe), potassium carbonate (99 %, BLD Pharm), sodium hydroxide (> 98 %, Carl Roth) were used as received.

Hexamethylene diamine (HMDA, 98%, Sigma-Aldrich) was purified by vacuum distillation over NaOH pellets and was kept under argon before use.

Erythritol dicarbonate was prepared from *meso*-erythritol and diphenyl carbonate in full accordance with the procedure published by us previously[S1]. T_m = 172.1°C; ^{1}H NMR (600 MHz, DMSO-d_6, δ): 5.17 – 5.10 (m, 2H), 4.65 – 4.57 (m, 2H), 4.43 – 4.36 (m, 2H).

Solvents: tetrahydrofuran (THF, 99.6 %, Fisher Scientific), acetonitrile (> 99.5 %, Fisher Scientific), dichloromethane (DCM, > 99.5 %, Fisher Scientific), diethyl ether (99+ %, Fisher Scientific), 1-methyl-2-pyrrolidone (NMP, 99.5 %, Extra Dry, AcroSeal, Acros Organics), acetone (technical grade, Fisher Scientific), (99.9 %, Extra Dry over Molecular Sieve, AcroSeal™, Acros Organics), hexane, (99.5 %, Fisher Scientific), toluene (99+%, Fisher Scientific), N,N-Dimethylformamide (DMF, 99.8%, Extra Dry, AcroSeal, Acros Organics) were used as received.

Tetrahydrofuran (THF, 99.6 %, Fisher Scientific) and toluene (99+%, Fisher Scientific) were dried and degassed prior to use employing a solvent purification system (SPS-800, MBRAUN). Ultrapure deionized water was obtained using Arium® Comfort (Sartorius) smart station.

NMR solvents and standards: dimethyl sulfoxide-d_6 (DMSO-d_6, 99.9 atom%D, Sigma-Aldrich) was dried over 3Å molecular sieves.

LSC-PV assembly: monocrystalline high efficiency silicon solar cells were provided by IXYS (IXOLAR SolarBIT KXOB25-12X1L active area = 2.2 × 0.6 cm^2, V_{OC} = 0.67 ± 0.01 V, J_{SC} = 53.60 ± 0.42 mA cm^{-2}, FF = 69.4 ± 0.3%, power conversion efficiency (PCE) = 24.69 ± 0.23%).

II. Methods

I.2.1. Nuclear magnetic resonance (NMR) spectra were recorded on Avance III HD 600MHz (Bruker) spectrometer (^{1}H NMR at 600 MHz, ^{13}C NMR at 151 MHz) at 25°C, unless otherwise stated, using the indicated deuterated solvent. Chemical shifts are reported in parts per million (ppm). Residual proton and carbon signals of the deuterated solvents were used as internal references for ^{1}H and ^{13}C NMR, respectively. Signals from common non-deuterated solvents and impurities were identified according to *Fulmer et al* [S2].

I.2.2. Determination of the degree of modification of PHU polymers using ^{1}H NMR was performed following the general method reported in literature[S1].

The degrees of modification of the **PHU-Ph** series polymers were determined from the ratio of the integrated signals in the 7.46–7.28 ppm region, corresponding to five aromatic protons of the phenyl group, to the signal at 2.95 ppm, assigned to four protons of two symmetrical -CH_2- groups in the PHU backbone.

For **PHU-Flu**, the degree of modification was calculated using the ratio of the integrated signals in the 8.07–6.63 ppm region, attributed to eleven aromatic protons of the aldehyde moiety (contributions from the two NH protons of the PHU backbone in this region were excluded from the calculation) to the signal at 2.94 ppm, corresponding to four protons of two symmetrical -CH_2- groups in the PHU backbone.

For **PHU-Coum**, the degree of modification was determined from the ratio of the integrated signal at 6.35–6.21 ppm, corresponding to one proton of the coumarin unit (see Fig. S4), to the signal at 2.94 ppm, assigned to four protons of two symmetrical -CH_2- groups in the PHU backbone.

I.2.3. Size exclusion chromatography (SEC) / gel permeation chromatography (GPC) was used to determine the number-average molecular weights ($M_{n(GPC)}$) and M_w/M_n ratios. The study was performed on a 1200 Infinity gel permeation chromatograph (Agilent Technologies, USA) equipped with PLgel 5µm MIXED-D column (Agilent Technologies, USA), PLgel 5µm (Agilent Technologies) pre-column and an integrated refractive index detector. The system was operated at 50°C and 1.0 mL/min flow using 0.1 M $Li(CF_3SO_2)_2N$ (LiTFSI) solution in DMF as an eluent. Poly(methyl methacrylate) standards (EasiVial PM, Agilent Technologies, M_p = 550 - 1558×10^3) were used to perform calibration.

Degree of polymerization (D_{pn}) was calculated with the GPC data using the following formula:

$$D_{pn} = {}^{M_{n(GPC)}}\!/_{(M_{ED} + M_{HMDA})} \quad \text{(S1)}$$

where $M_{n(GPC)}$ is the number average molecular weight of PHU polymer determined using GPC, M_{ED} is the molecular weight of erythritol dicarbonate monomer and M_{HMDA} is the molecular weight of hexamethylene diamine used in the synthesis of PHU polymer.

I.2.4. Thermal gravimetric analysis (TGA) was carried out in air on a TGA2 STARe System (Mettler Toledo) applying a heating rate of 5°C/min. The onset weight loss temperature (T_{onset}) was determined as the point in the TGA curve at which a significant deviation from the horizontal was observed. The resulting temperature was then rounded to the nearest 5°C.

I.2.5. Differential Scanning Calorimetry (DSC) measurements were performed using a DSC 300 Caliris Select calorimeter (NETZSCH). For aldehydes $\mathbf{A_1}$ and $\mathbf{A_2}$, two heating–cooling cycles were conducted for each sample at a heating rate of 5 °C/min under a nitrogen atmosphere. Melting temperatures (T_m) were determined from the first heating scan. The glass-transition temperature (T_g) and crystallization temperature (T_{cr}) of $\mathbf{A_2}$ were identified from the second heating scan, whereas the T_{cr} of $\mathbf{A_1}$ was determined from the second cooling scan. For simplicity, both T_m and T_{cr} values were taken as the peak maxima. For **PHU_1-Flu** and **PHU_1-Coum**, three heating–cooling cycles were performed under a nitrogen atmosphere: the first two cycles were recorded at a rate of 5 °C/min, followed by a third cycle at 10 °C/min. The T_g and T_m were determined from the first heating scan.

I.2.6. UV-vis spectrophotometry was performed using a Thermo Scientific Evolution 600 UV–vis spectrophotometer, recording both absorption and transmission spectra. Solution measurements were carried out on polymer solutions in DMF with concentrations of approximately 10^{-7} M. Thin films were prepared by spin-coating 10 wt% PHU solutions in DMF at 900 rpm for 60 s using a Laurell WS-400BZ-6NPP/LITE spin coater. Films were deposited either onto 2.5 × 2.5 cm² thin glass substrates for UV–vis measurements or onto 5.0 × 5.0 × 0.6 cm³ N-BK7 high-optical-quality glass slabs for LSCs fabrication.

I.2.7. Steady-state fluorescence spectroscopy was carried out on a Jasco FP-6600 spectrofluorometer. Photoluminescence (PL) spectra were recorded from quartz cuvettes containing polymer solutions in DMF (≈10^{-7} M) as well as from thin films prepared as described above.

I.2.8. Time-resolved fluorescence (TRF) spectroscopy was carried out using a NanoLog system equipped with an iH320 spectrograph, a PPD-850 single-photon detector module, and a DeltaTime series DD-405L DeltaDiode laser. Data analysis was performed using the DAS6 software. The photoluminescence quantum yields (PLQYs) of thin films were measured using a home-built integrating sphere following a previously reported procedure[S3]. The setup comprised a SPEX 270M monochromator coupled to a liquid-nitrogen-cooled charge-coupled device (CCD). Excitation was provided by a monochromated 450 W Xe lamp at 330 nm. All spectra were corrected for the instrumental response.

I.2.9. Photonic characterization was conducted by illuminating the top surface of the LSCs using an Abet Technologies Sun 2000 solar simulator equipped with an AM1.5G filter (irradiance = 1000 W m^{-2}). Edge-emitted photons were collected with an International Light Technologies ILT950 spectroradiometer fitted with a cosine corrector. Spectral data were acquired using SpectrLight III software, enabling the determination of the external and internal photon efficiencies (η_{ext} and η_{int}, respectively) as well as the absorption efficiency (η_{abs}). All measurements were performed against a black background to suppress back-reflections (prevent the double passage of transmitted photons) and avoid overestimation of device performance. Chromaticity coordinates were additionally measured in a front-face configuration.

I.2.10. Photovoltaic (PV) characterization was performed using a Keithley 2612B digital multimeter by applying voltage sweeps and recording the current output of the LSC-PV devices under 1 Sun AM1.5G top illumination provided by the same solar simulator used for photonic characterization. Two opposite edges of the glass substrate were optically coupled to the photoactive regions of monocrystalline silicon PV cells using a hot-melt ethylene-vinyl acetate (EVA) adhesive, while the remaining two edges were masked with black tape. All measurements were carried out against a black background to prevent double passage of transmitted photons through the device and consequent overestimation of the photovoltaic performance.

III. Synthesis and characterization of fluorescent aldehydes.

III.1. 4-(9H-fluoren-2-yl)benzaldehyde (**A_1**).

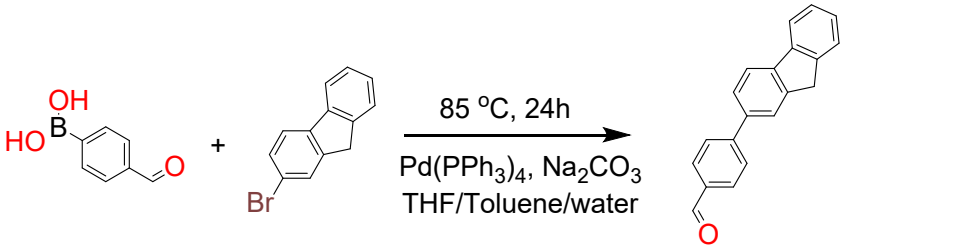

Scheme S1. Synthesis of 4-(9H-fluoren-2-yl)benzaldehyde (**A_1**).

The synthetic procedure was developed by combining and adapting three closely related methods reported in the literature[S4-S6]. Tetrahydrofuran (THF, 60 mL), toluene (80 mL), and water (20 mL) were introduced into a 250 mL Schlenk flask and degassed by bubbling argon through the solvent mixture for 10 min. Subsequently, (4-formylphenyl)boronic acid (3.67 g, 24.5 mmol), 2-bromo-9H-fluorene (5.00 g, 20.4 mmol), tetrakis(triphenylphosphine)palladium(0) (0.71 g, 0.61 mmol), and sodium carbonate (6.49 g, 61.2 mmol) were added, and the resulting mixture was stirred until complete dissolution of the reagents was achieved. The reaction mixture was then refluxed for 24 h under an inert argon atmosphere. Upon completion, the mixture was allowed to cool to room temperature and transferred to a 500 mL round-bottom flask. The organic solvents were removed under reduced pressure using a rotary evaporator, after which the residue was diluted with water (150 mL) and extracted with dichloromethane (DCM, 3 × 100 mL). The combined organic phases were washed with brine (50 mL) and dried over anhydrous magnesium sulfate overnight. After removal of the drying agent by filtration, the solvent was evaporated to dryness. The resulting crude solid was crystallized from a 1:2 (v/v) acetone/hexane mixture (150 mL acetone and 300 mL hexane) by cooling in a freezer at -18 °C. The formed crystals were collected by filtration and washed with cold hexane. The final product was obtained after a second recrystallization at -18 °C from a minimal amount of hot acetone, yielding a yellow powder. It was isolated by filtration, washed with hexane and dried at 60°C in vacuum (<1 mbar) for 6 hours. Yield: 5.1 g (92.5%). Anal. calcd. for $C_{20}H_{14}O$ (270.33): C, 88.86%; H, 5.22%. Found: C, 88.45%; H, 5.31%; ^{1}H NMR (600 MHz, DMSO-d_6) δ = 10.06 (s, 1H), 8.07 – 7.95 (m, 7H), 7.82 (dd, J = 8.0, 1.8 Hz, 1H), 7.63 (d, J = 7.4 Hz, 1H), 7.39 (dtd, J = 36.3, 7.4, 1.1 Hz, 2H), 4.02 (s, 2H). T_m (DSC, 5°C/min) = 194.6°C; T_c (DSC, 5°C/min) = 174.8°C; T_{onset} (TGA, 5°C/min, on air) = 205°C.

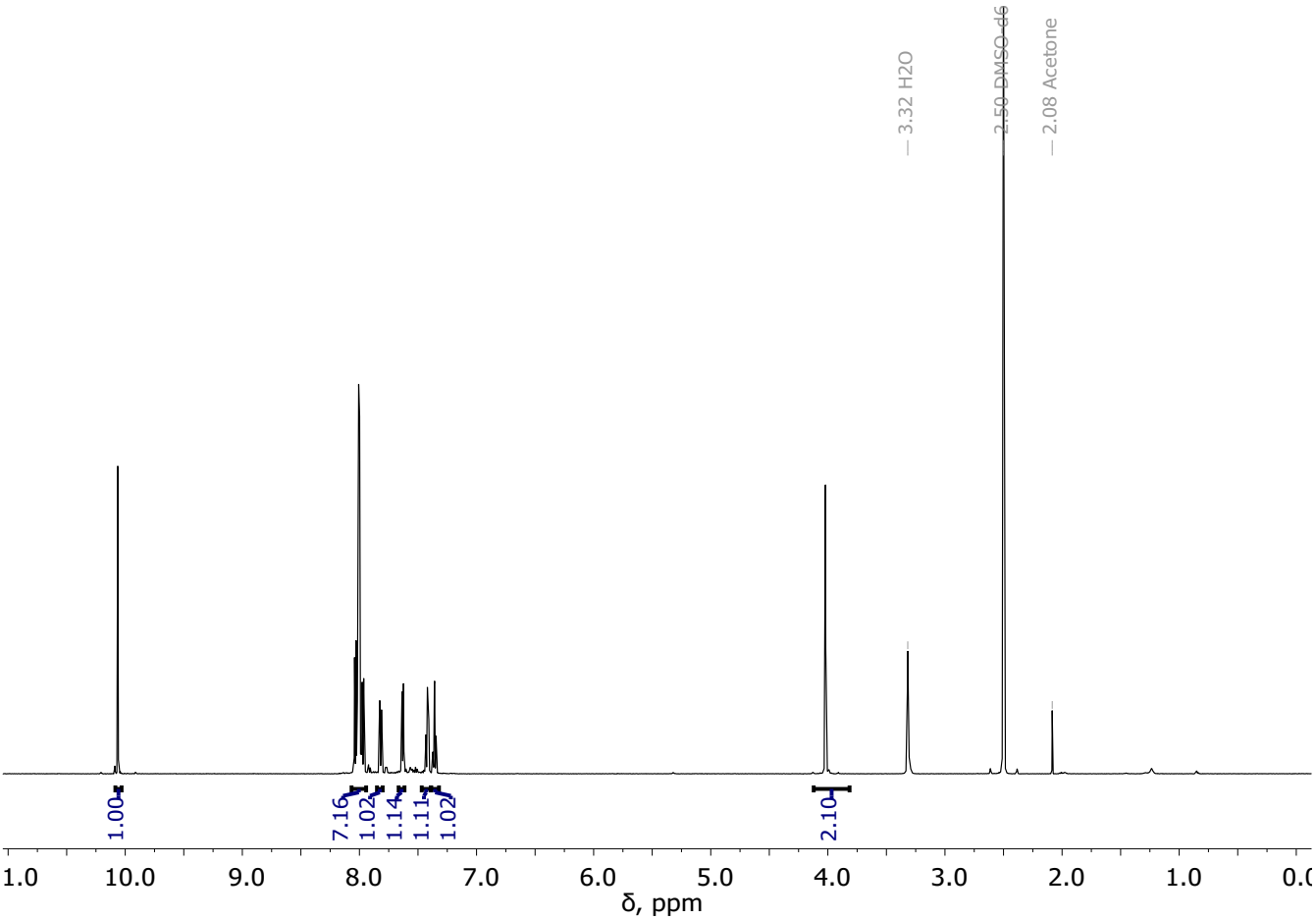

Figure S1. ^{1}H NMR spectrum of $\mathbf{A_1}$ in DMSO-d_6.

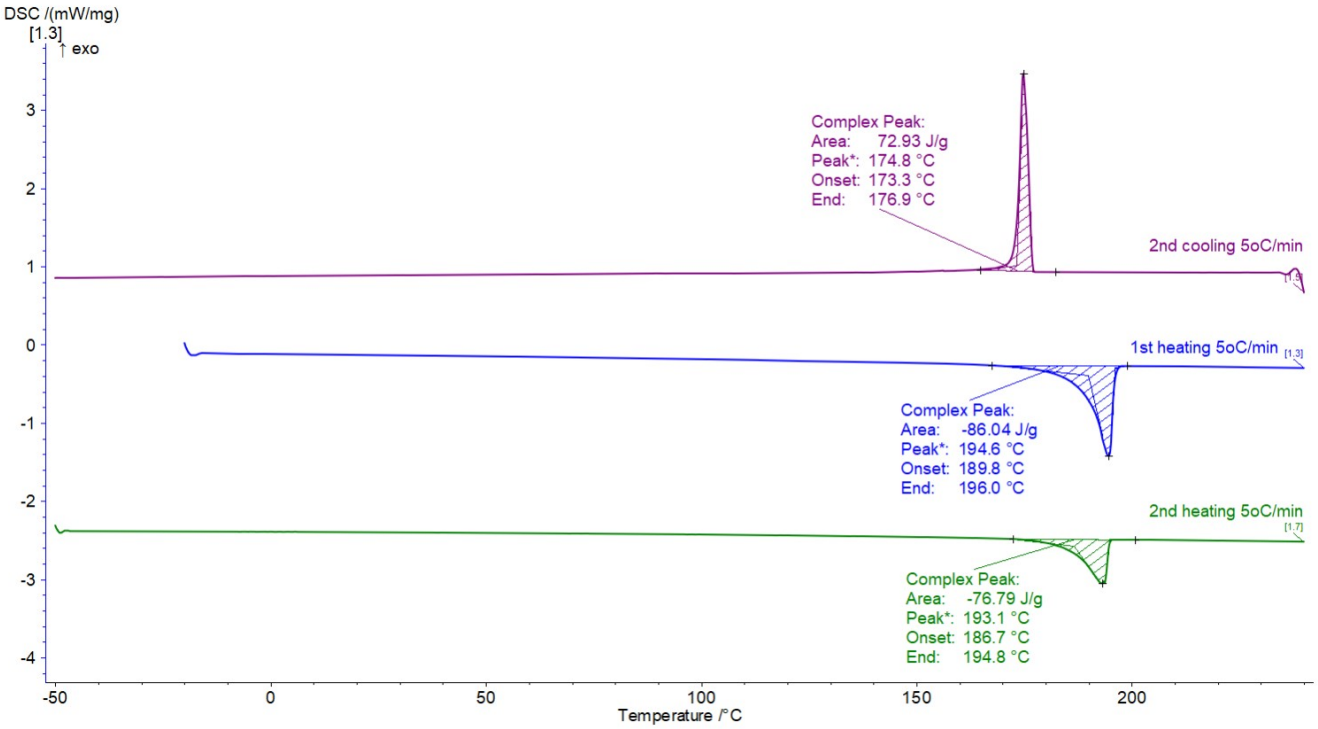

Figure S2. DSC plots of $\mathbf{A_1}$.

III.2. 4-(2-((2-oxo-2H-chromen-7-yl)oxy)ethoxy)benzaldehyde (**A_2**).

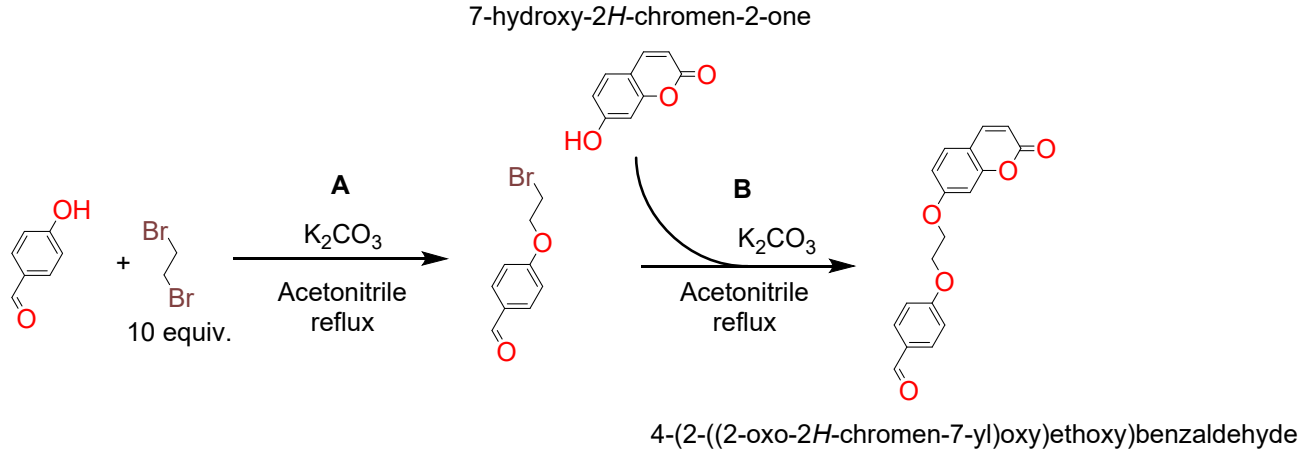

Scheme S2. Synthesis of 4-(2-((2-oxo-2H-chromen-7-yl)oxy)ethoxy)benzaldehyde (**A_2**).

The synthetic procedure was created using previously developed synthetic protocols for similar compounds[S7-S8].

A. Synthesis of 4-(2-bromoethoxy)benzaldehyde.

4-Hydroxybenzaldehyde (6.50 g, 52.2 mmol) was introduced into a 500 mL round-bottom flask and dissolved in acetonitrile (250 mL). Potassium carbonate (14.71 g, 106.5 mmol) and 1,2-dibromoethane (100.00 g, 532.3 mmol, 10.0 equiv.) were then added sequentially. The resulting suspension was refluxed for 20 h under vigorous stirring. After cooling to room temperature, the reaction mixture, including suspended solids, was transferred to a 1 L separatory funnel. Water (400 mL) was added, and the mixture was shaken thoroughly to ensure homogenization. The aqueous phase was extracted with diethyl ether (2 × 200 mL). The combined organic layers were washed with brine (60 mL) and dried over anhydrous magnesium sulfate overnight. After removal of the drying agent by filtration, the solvent was evaporated under reduced pressure to afford a brownish crude solid. Purification was achieved by vacuum distillation (0.45 mbar), allowing separation of 4-(2-bromoethoxy)benzaldehyde from the major by-product, 4,4′-(ethane-1,2-diylbis(oxy))dibenzaldehyde. The isolated product was obtained as a colorless oil, which slowly crystallized upon cooling to room temperature to yield white-to-pale-yellow crystals of 4-(2-bromoethoxy)benzaldehyde. Yield: 11.17 g (91.6 %). ^{1}H NMR (600 MHz, DMSO-d_6) δ = 9.88 (s, 1H), 7.92 – 7.82 (m, 2H), 7.20 – 7.11 (m, 2H), 4.45 (t, J = 5.4 Hz, 2H), 3.84 (dd, J = 6.1, 4.6 Hz, 2H).

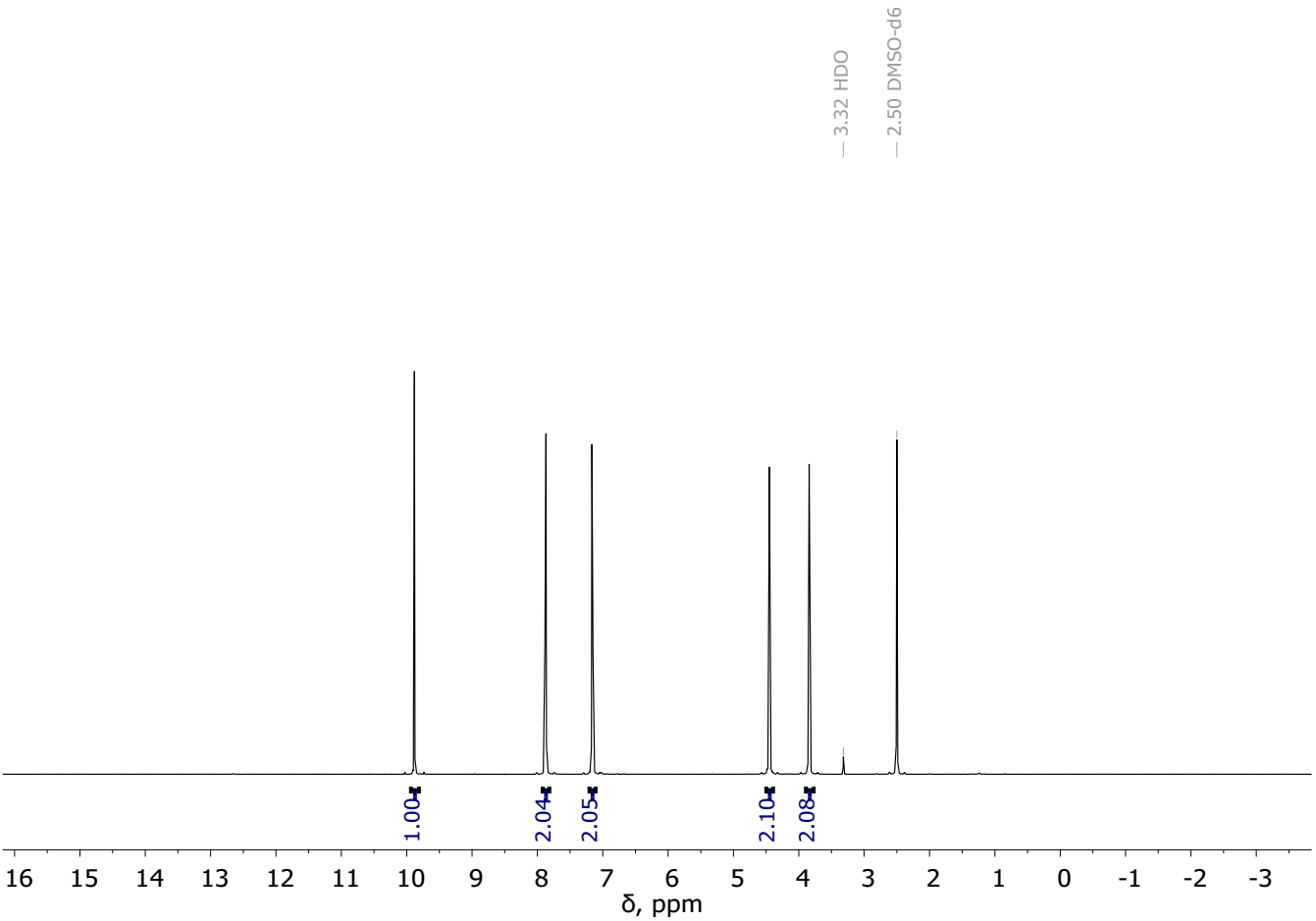

Figure S3. ^{1}H NMR spectrum of 4-(2-bromoethoxy)benzaldehyde in DMSO-d_6.

B. Synthesis of 4-(2-((2-oxo-2H-chromen-7-yl)oxy)ethoxy)benzaldehyde (A_2).

The synthetic procedure followed the protocol described above for compound $\mathbf{A_1}$. 4-(2-Bromoethoxy)benzaldehyde (5.00 g, 21.8 mmol), 7-hydroxy-2H-chromen-2-one (3.54 g, 21.8 mmol), and potassium carbonate (6.03 g, 43.7 mmol) were employed as starting materials. After completion of the reaction, the crude solid was isolated and purified by recrystallization from hot acetone with the gradual addition of diethyl ether. Once the boiling solution became slightly turbid, it was allowed to cool to room temperature and subsequently placed in a freezer at -18 °C. After 12 h, the dark-orange crystalline precipitate was collected by filtration, washed with diethyl ether, and dried under vacuum (<1 mbar) at 60 °C for 6 h. Yield: 3.5 g (51.7%). Anal. calcd. for $C_{18}H_{14}O_5$ (310.31): C, 69.67%; H, 4.55%. Found: C, 69.60%; H, 4.58%; ^{1}H NMR (600 MHz, DMSO-d_6) δ = 9.88 (s, 1H), 8.00 (d, J = 9.5 Hz, 1H), 7.92 – 7.84 (m, 2H), 7.65 (d, J = 8.6 Hz, 1H), 7.24 – 7.16 (m, 2H), 7.08 (d, J = 2.5 Hz, 1H), 7.01 (dd, J = 8.6, 2.5 Hz, 1H), 6.31 (d, J = 9.4 Hz, 1H), 4.48 (s, 4H); T_m (DSC, 5°C/min) = 160.1°C; T_{cr} (DSC, 5°C/min, on heating) = 58.2°C.

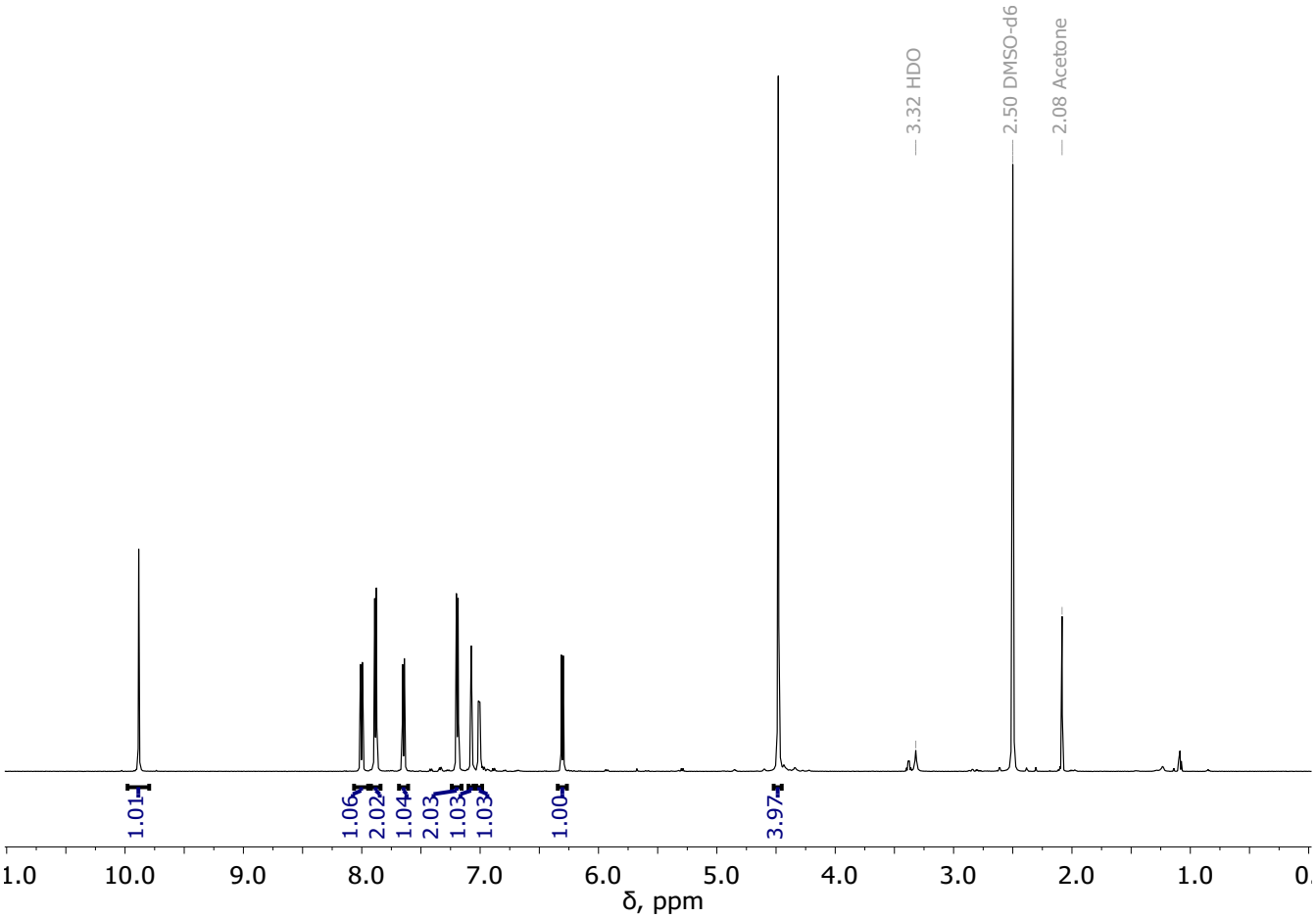

Figure S4. ^{1}H NMR spectrum of $\mathbf{A_2}$ in DMSO-d_6.

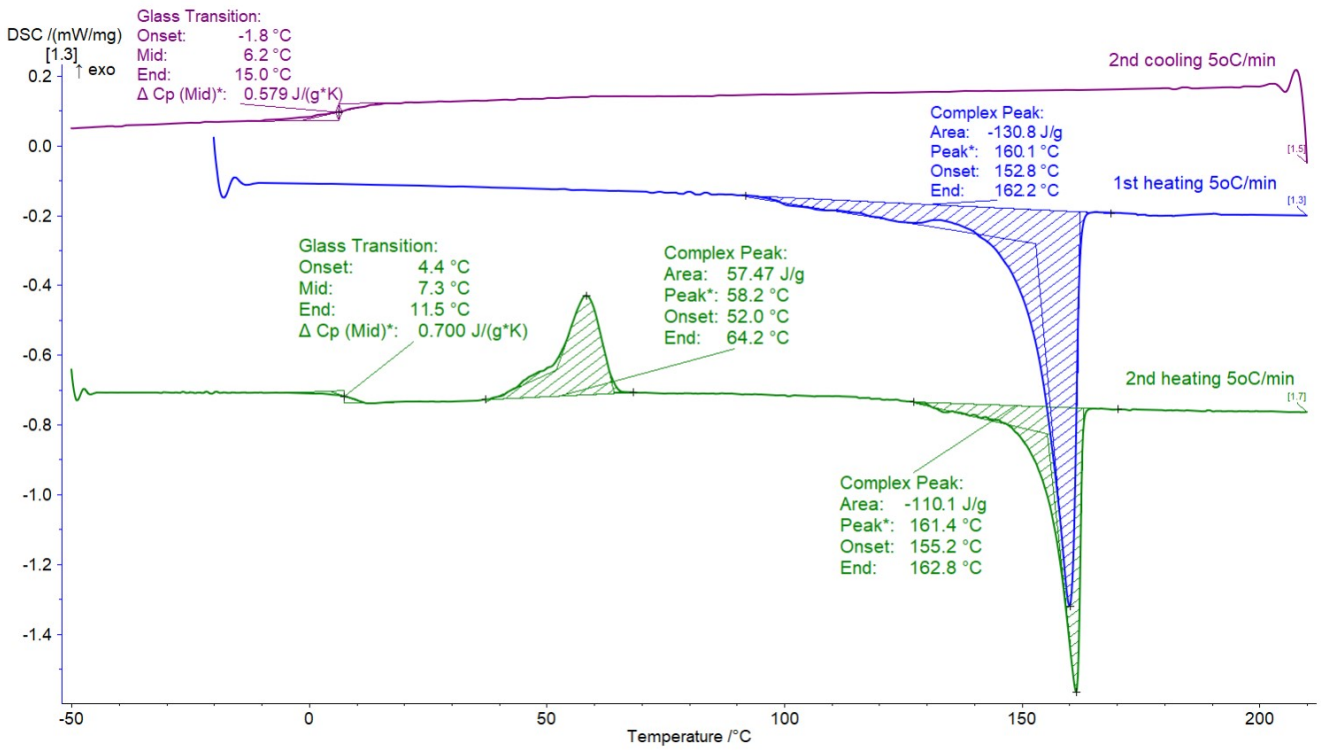

Figure S5. DSC plots of $\mathbf{A_2}$.

IV. Synthesis of PHU polymers.

IV.1. Synthesis of unmodified PHU (**PHU$_1$**).

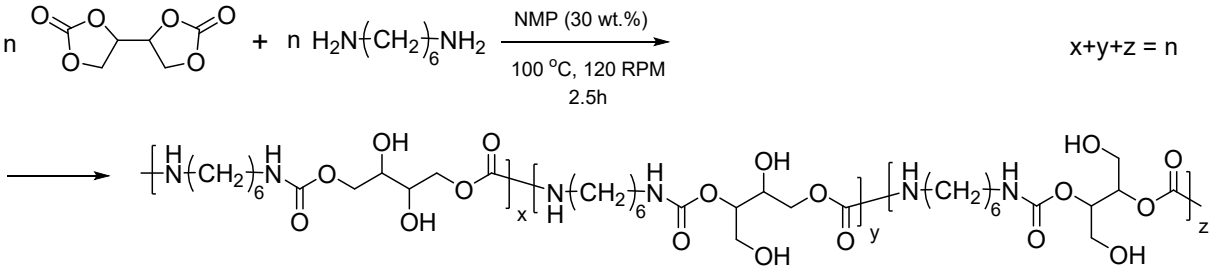

Scheme S3. Synthesis of **PHU$_1$** polymer.

Polyhydroxyurethane (PHU$_1$) derived from erythritol decarbonate (EDC) (8.00 g, 45.9 mmol) and hexamethylene diamine (HMDA) (5.34 g, 45.9 mmol) was synthesized in a twin-screw microcompounder Xplore MC15 according to the previously reported procedure[1]. Yield: 7.72 g (57.9 %); M_n (GPC) = 12500, M_w/M_n = 8.53.

IV.2. Optimization of procedure for **PHU$_1$** modification using benzaldehyde.

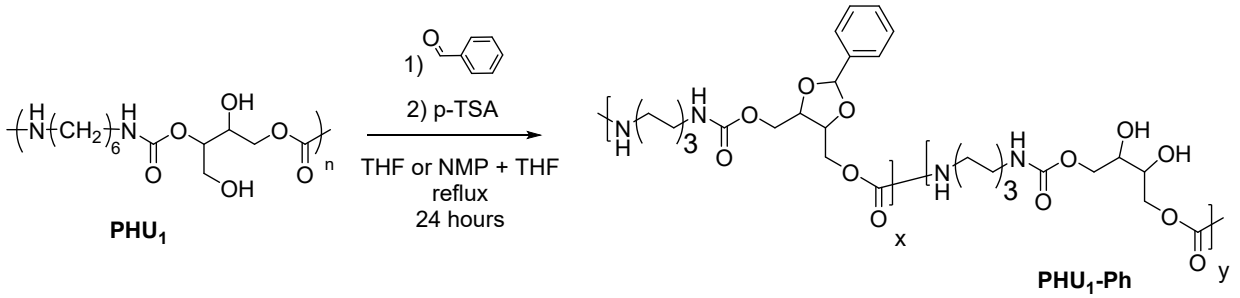

Scheme S4. Simplified scheme of synthesis of **PHU$_1$-Ph** polymer.

A. Synthesis using THF as a solvent.

PHU$_1$ polymer (1.00 g, 3.44 mmol) was placed in a 250 mL round-bottom flask and dissolved in THF (90 mL). *p*-Toluenesulfonic acid monohydrate (0.17 g, 0.91 mmol) was added in one portion, followed by benzaldehyde (1.43 g, 13.45 mmol). The resulting mixture was refluxed for 24 h using a 30 mL Soxhlet extractor filled with 4 Å molecular sieves to continuously remove water formed during the reaction. Over the course of the reaction, gradual dissolution of the polymer was visually observed. After cooling to room temperature, triethylamine (0.5 mL) was added to neutralize the residual *p*-toluenesulfonic acid. The reaction mixture was then precipitated into deionized water (200 mL). Partial gel formation was observed during precipitation. The combined precipitates were collected, air-dried for 2 h, and subsequently redissolved in THF. The resulting **PHU$_1$-Ph-A** polymer was only partially soluble, likely due to partial cross-linking. The soluble fraction was reprecipitated into diethyl ether, collected by filtration, and dried under vacuum (<1 mbar) at 80 °C for 12 h.

Modification degree: 93%, determined by ^{1}H NMR spectroscopy from the ratio of the aromatic proton signals of the phenyl group (7.46–7.28 ppm) to the methylene (–CH$_2$–) signal at 2.95 ppm, according to the method reported previously[S1].

^{1}H NMR (600 MHz, DMSO-d$_6$) δ 7.46 – 7.28 (m, 5H), 7.28 – 6.67 (m, 2H), 6.13 – 3.47 (m, 8H), 2.95 (dd, *J* = 14.4, 6.9 Hz, 4H), 1.44 – 1.31 (s, 4H), 1.23 (s, 4H).

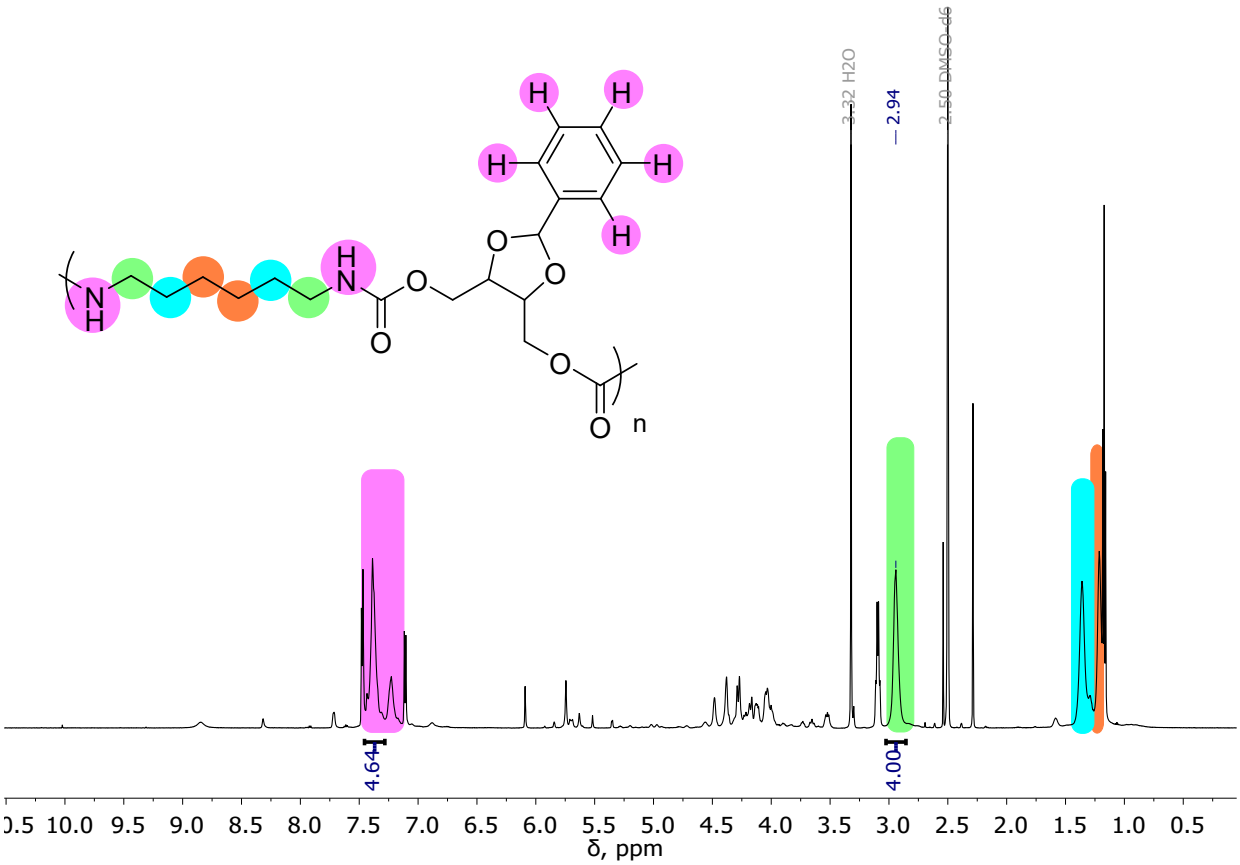

Figure S6. ^{1}H NMR spectrum of **PHU$_1$-Ph-A** in DMSO-d$_6$.

B. Synthesis using acetonitrile (can) as a solvent.

The synthesis was performed following the same procedure as described in **A**, with acetonitrile (90 mL) used in place of THF. The resulting **PHU$_1$-Ph-B** polymer was only partially soluble, presumably due to partial cross-linking. The soluble fraction was precipitated into diethyl ether, collected by filtration, and dried under vacuum (<1 mbar) at 80 °C for 12 h. Yield: 0.43 g (33.0%). M_n (GPC) = 15800, M_w/M_n = 31.1.

Modification degree: 91%, determined by ^{1}H NMR spectroscopy from the ratio of the aromatic proton signals of the phenyl group (7.46–7.28 ppm) to the methylene (–CH$_2$–) signal at 2.95 ppm.

^{1}H NMR (600 MHz, DMSO-d$_6$) δ 7.46 – 7.28 (m, 5H), 7.28 – 6.67 (m, 2H), 6.13 – 3.47 (m, 8H), 2.95 (dd, *J* = 14.4, 6.9 Hz, 4H), 1.44 – 1.31 (s, 4H), 1.23 (s, 4H).

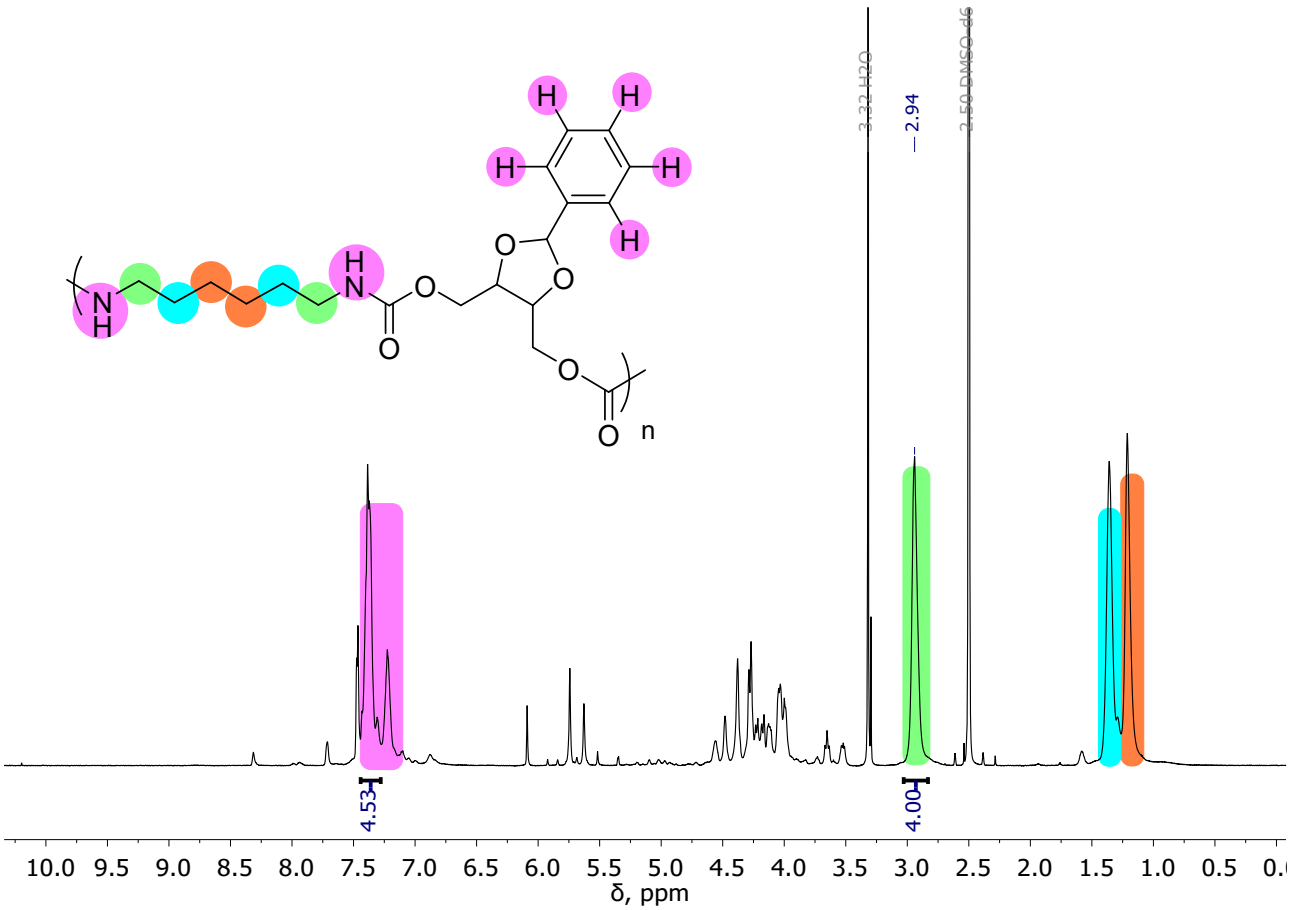

Figure S7. ^{1}H NMR spectrum of **PHU$_1$-Ph-B** in DMSO-d$_6$.

C. Synthesis using a mixture of NMP and THF (1:2, v/v) as a solvent.

PHU$_1$ polymer (1.07 g, 3.69 mmol) was placed in a 250 mL round-bottom flask and dissolved in anhydrous *N*-methyl-2-pyrrolidone (NMP, 30 mL). Tetrahydrofuran (THF, 60 mL) was then added dropwise to prevent polymer precipitation. Subsequently, *p*-toluenesulfonic acid monohydrate (0.17 g, 0.91 mmol) was added in one portion, followed by benzaldehyde (1.43 g, 13.45 mmol). The resulting solution was refluxed for 24 h using a 30 mL Soxhlet extractor filled with 4 Å molecular sieves to continuously remove water formed during the reaction. After cooling to room temperature, triethylamine (0.5 mL) was added to neutralize the residual *p*-toluenesulfonic acid. The polymer was then precipitated into deionized water (200 mL). The resulting precipitate was collected, air-dried for 2 h, and subsequently redissolved in THF until a homogeneous polymer solution was obtained. The **PHU$_1$-Ph-C** was finally precipitated into diethyl ether, collected by filtration, and dried under vacuum (<1 mbar) at 80 °C for 12 h. Yield: 1.12 g (93.0%).

Modification degree: 91%, determined by ^{1}H NMR spectroscopy from the ratio of the aromatic proton signals of the phenyl group (7.46–7.28 ppm), corrected by subtracting five times the integral of the aldehyde proton signal at 10.02 ppm (corresponding to unreacted aldehyde), to the methylene (-CH$_2$-) signal at 2.95 ppm.

^{1}H NMR (600 MHz, DMSO-d$_6$) δ 7.46 – 7.28 (m, 5H), 7.28 – 6.67 (m, 2H), 6.13 – 3.47 (m, 8H), 2.95 (dd, *J* = 14.4, 6.9 Hz, 4H), 1.44 – 1.31 (s, 4H), 1.23 (s, 4H).

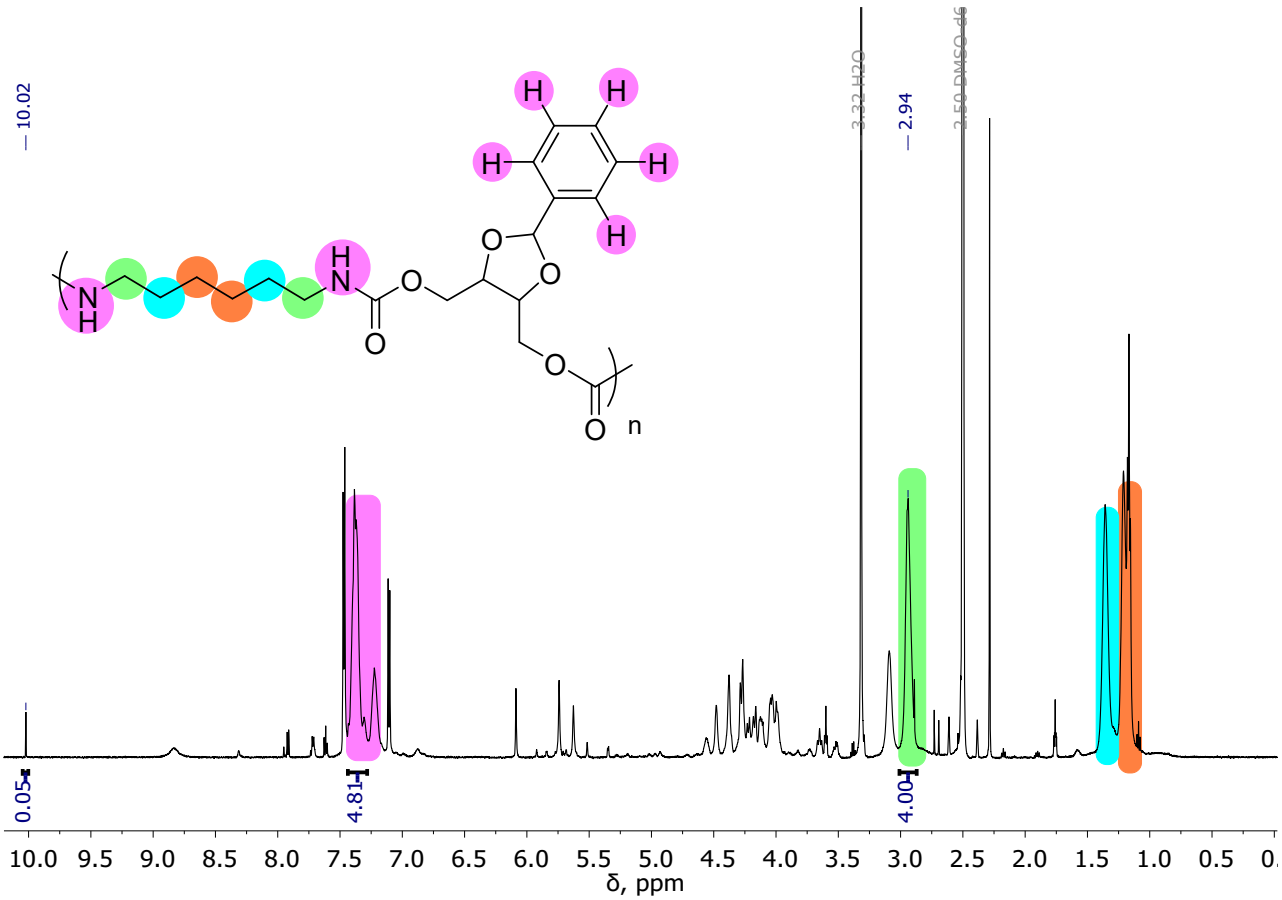

Figure S8. ^{1}H NMR spectrum of **PHU$_1$-Ph-C** in DMSO-d$_6$

IV.3. Synthesis of **PHU$_1$** modified with 4-(9H-fluoren-2-yl)benzaldehyde (**PHU$_1$-Flu**).

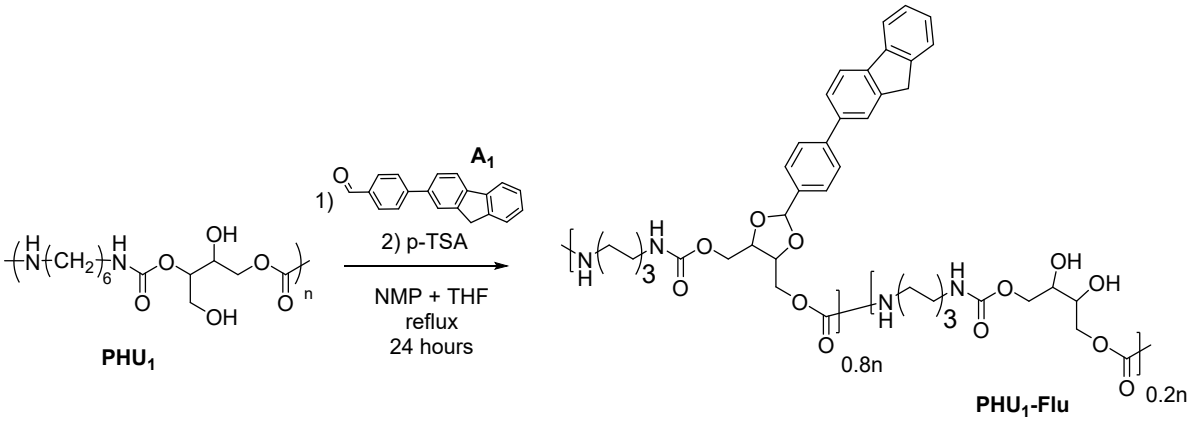

Scheme S5. Simplified scheme of synthesis of **PHU$_1$-Flu** polymer.

PHU$_1$ polymer (1.07 g, 3.69 mmol) was introduced into a 250 mL round-bottom flask and dissolved in anhydrous *N*-methyl-2-pyrrolidone (NMP, 30 mL). Tetrahydrofuran (THF, 60 mL) was then added dropwise to prevent polymer precipitation. Subsequently, 4-(9H-fluoren-2-yl)benzaldehyde (4.00 g, 14.79 mmol) and *p*-toluenesulfonic acid monohydrate (0.19 g, 1.00 mmol) were added in one portion. The resulting solution was refluxed for 24 h using a 30 mL Soxhlet extractor filled with 4 Å molecular sieves to continuously remove water generated during the reaction. After cooling to room temperature, triethylamine (0.5 mL) was added to neutralize the residual acid. The reaction mixture was then precipitated into deionized water (200 mL); however, partial co-precipitation of unreacted aldehyde was observed. The crude precipitate was therefore transferred to a 100 mL Soxhlet extractor and extracted with hot THF. Under these conditions, both the modified polymer and residual aldehyde were soluble in THF and were collected in the receiving round-bottom flask, while small amounts of insoluble material remained in the Soxhlet thimble. After cooling to room temperature, the solvent was removed under reduced pressure, and

the resulting solid was subjected to a second Soxhlet extraction using hot dichloromethane to selectively remove the unreacted aldehyde. The purified **PHU$_1$-Flu** polymer was collected and dried under vacuum (<1 mbar) at 80 °C for 12 h. Yield: 1.237 (61.7 %). M_n (GPC) = 17000, M_w/M_n = 12.9; T_m (DSC, 5°C/min) = 143.8°C, T_m (DSC, 10°C/min) = 146.1°C, T_c (DSC, 5°C/min) = 136.3°C, T_c (DSC, 10°C/min) = 132.4°C; T_{onset} (TGA, 5°C/min, air) = 235°C.

Modification degree: 80%, determined by ^{1}H NMR spectroscopy from the ratio of the integrated signals at 8.07–6.63 ppm to the signal at 2.94 ppm. The aromatic region (8.07–6.63 ppm) corresponds to 11 aromatic protons from the aldehyde moiety and to the two NH protons of the PHU backbone, which also resonate in this region; the later were excluded from the calculation. The signal at 2.94 ppm corresponds to four methylene protons of the PHU backbone and was used as the internal reference.

^{1}H NMR (600 MHz, DMSO-d$_6$) δ 8.07 – 6.63 (m, 11H), 6.17 – 5.52 (m, 1H), 5.28 – 3.43 (m, 8H), 2.94 (s, 4H), 1.36 (s, 4H), 1.21 (s, 4H).

^{13}C NMR (151 MHz, DMSO-d$_6$) δ 155.89, 155.81, 155.77, 143.85, 143.28, 140.66, 138.22, 127.63, 126.94, 126.88, 126.81, 126.54, 126.50, 126.31, 125.60, 125.55, 125.15, 123.44, 120.40, 120.13, 75.31, 62.66, 54.91, 40.22, 36.47, 29.32, 29.16, 25.94.

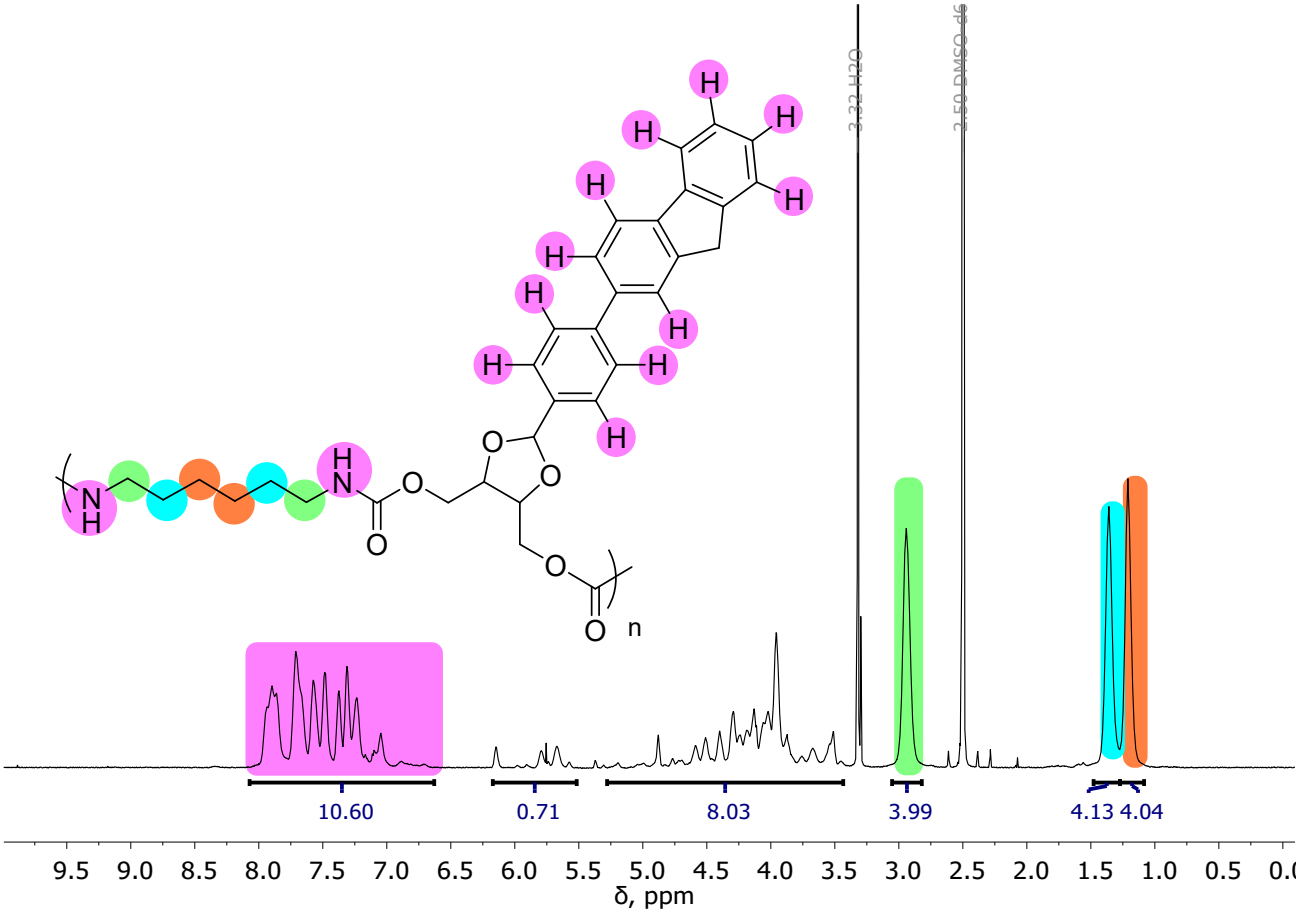

Figure S9. ^{1}H NMR spectrum of **PHU$_1$-Flu** in DMSO-d$_6$.

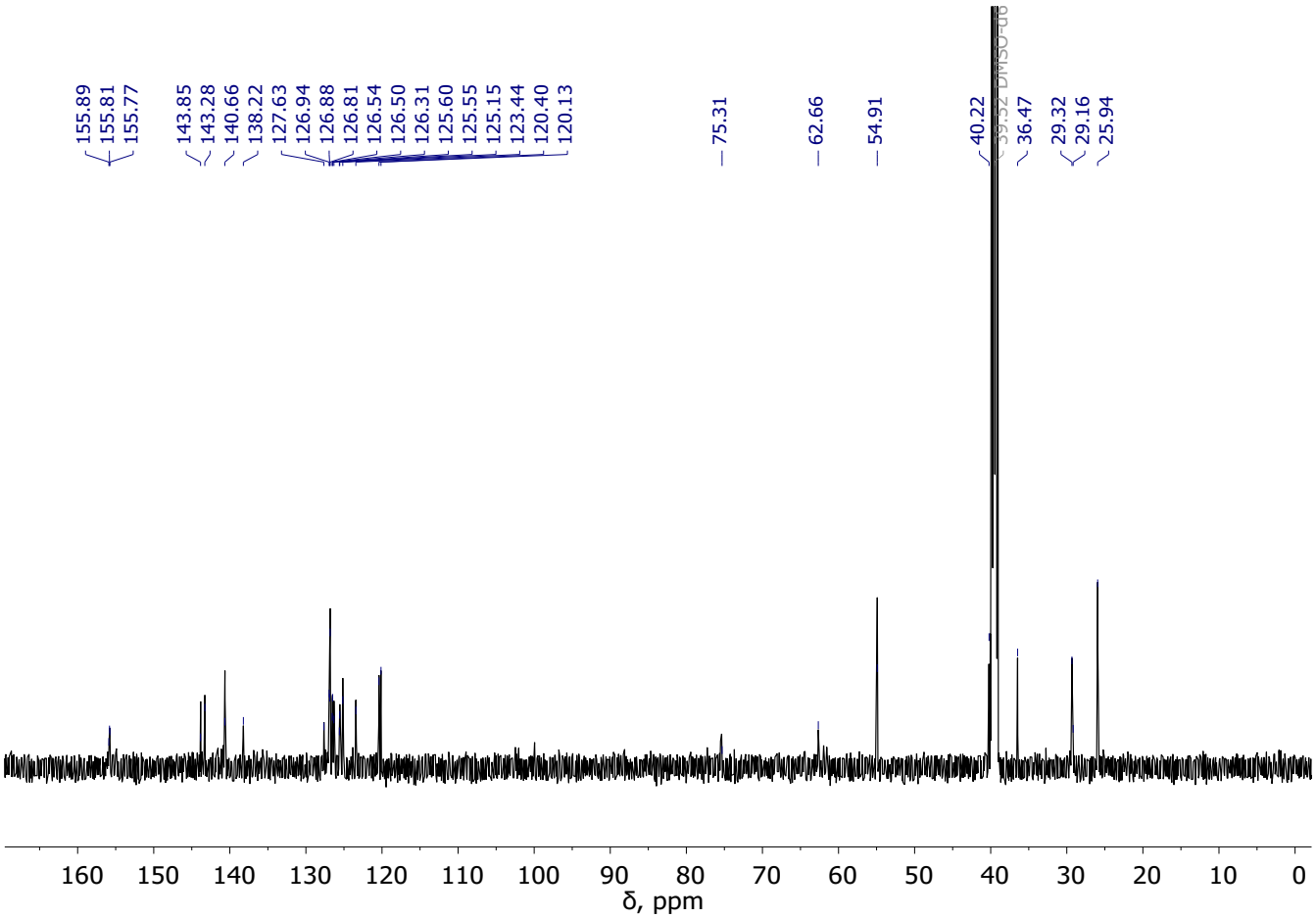

Figure S10. ^{13}C NMR spectrum of **PHU$_1$-Flu** in DMSO-d$_6$.

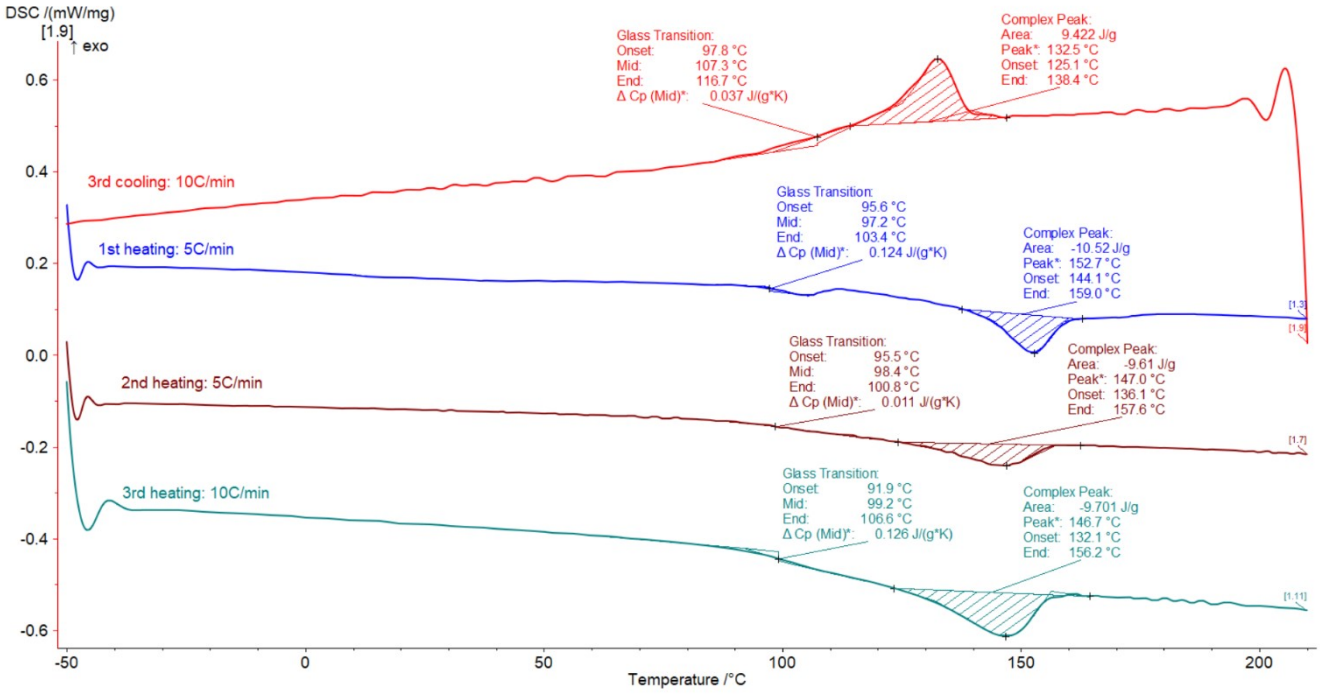

Figure S11. DSC plots of **PHU$_1$-Flu**.

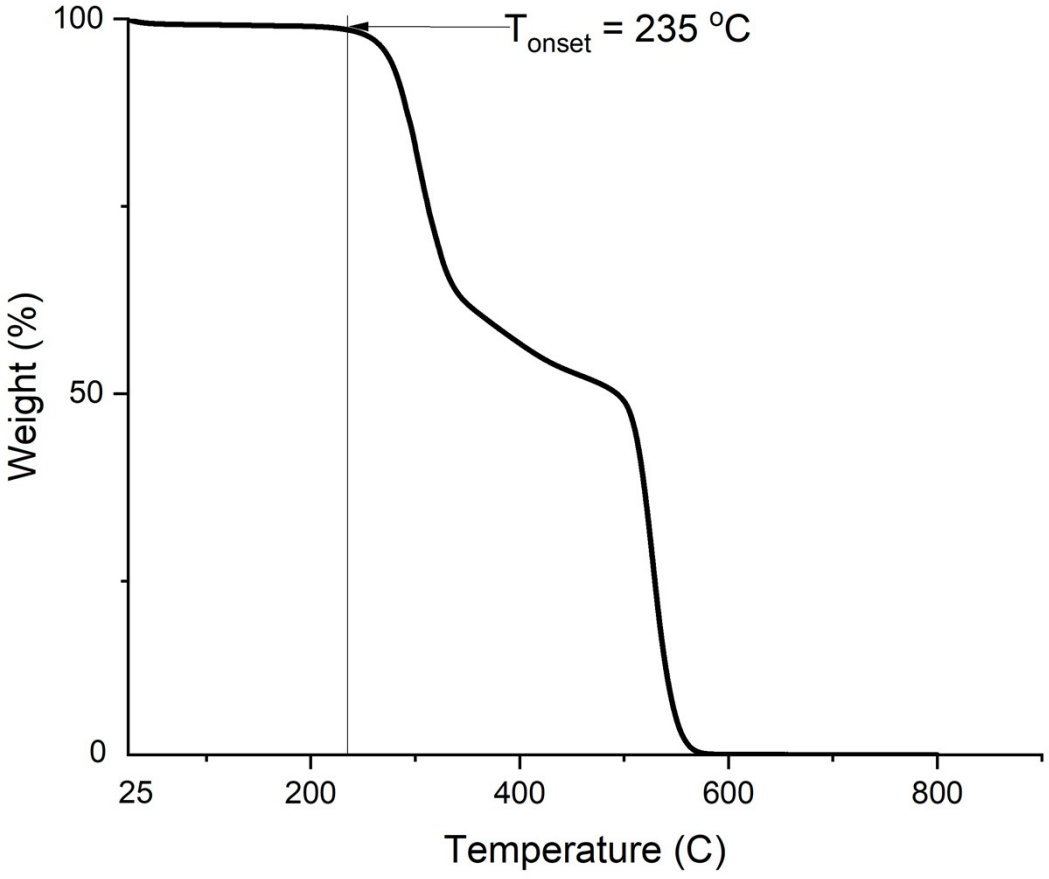

Figure S12. TGA plot of **PHU$_1$-Flu**.

IV.4. Synthesis of **PHU$_1$** modified with 4-(2-((2-oxo-2H-chromen-7-yl)oxy)ethoxy)benzaldehyde (**PHU$_1$-Coum**).

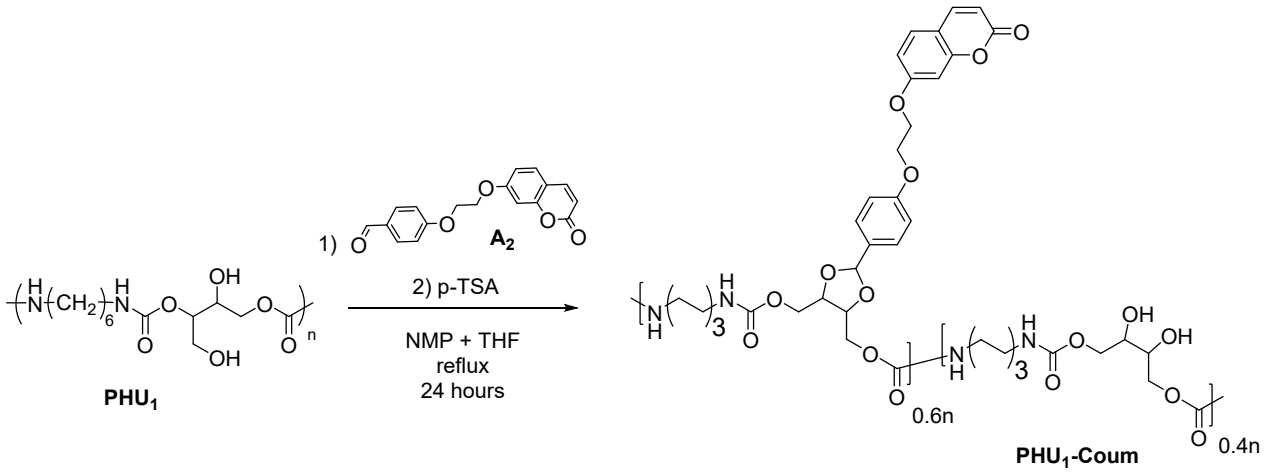

Scheme S6. Simplified scheme of synthesis of modified **PHU$_1$-Coum** polymer.

PHU$_1$-Coum was synthesized following the same procedure as **PHU$_1$-Flu** using **PHU$_1$** polymer (0.61 g, 2.1 mmol), 4-(2-((2-oxo-2H-chromen-7-yl)oxy)ethoxy)benzaldehyde (2.61 g, 8.41 mmol), and *p*-toluenesulfonic acid monohydrate (0.11 g, 0.57 mmol). Yield: 0.61 g (49.8 %). M_n (GPC) = 22400, M_w/M_n = 6.4; T_g (DSC, 5°C/min) = 59.5°C, T_g (DSC, 10°C/min) = 59.8°C; T_{onset} (TGA, 5°C/min, air) = 220°C.

Modification degree: 60%, calculated by ^{1}H NMR spectroscopy from the ratio of the signal at 6.35–6.21 ppm, assigned to one proton of the coumarin moiety (see Fig. S4), to the methylene signal of the PHU backbone at 2.94 ppm (four protons).

^{1}H NMR (600 MHz, DMSO-d$_6$) δ 7.97 (s, 1H), 7.62 (s, 1H), 7.45 – 6.87 (m, 6H), 6.35 – 6.21 (m, 1H), 4.95 – 3.45 (m, 10H), 2.94 (s, 4H), 1.36 (d, J = 11.7 Hz, 4H), 1.21 (s, 4H).
^{13}C NMR (151 MHz, DMSO-d$_6$) δ 161.44, 160.25, 159.13, 158.56, 156.49, 155.88, 155.77, 155.35, 154.91, 144.27, 130.22, 129.52, 129.24, 128.58, 128.02, 127.90, 127.63, 125.49, 114.14, 113.98, 113.89, 112.74, 112.62, 112.52, 102.56, 101.30, 100.02, 77.20, 75.32, 75.22, 69.93, 67.72, 67.09, 66.13, 65.79, 62.66, 61.99, 50.54, 29.41, 29.32, 29.18, 25.96, 22.13, 20.77.

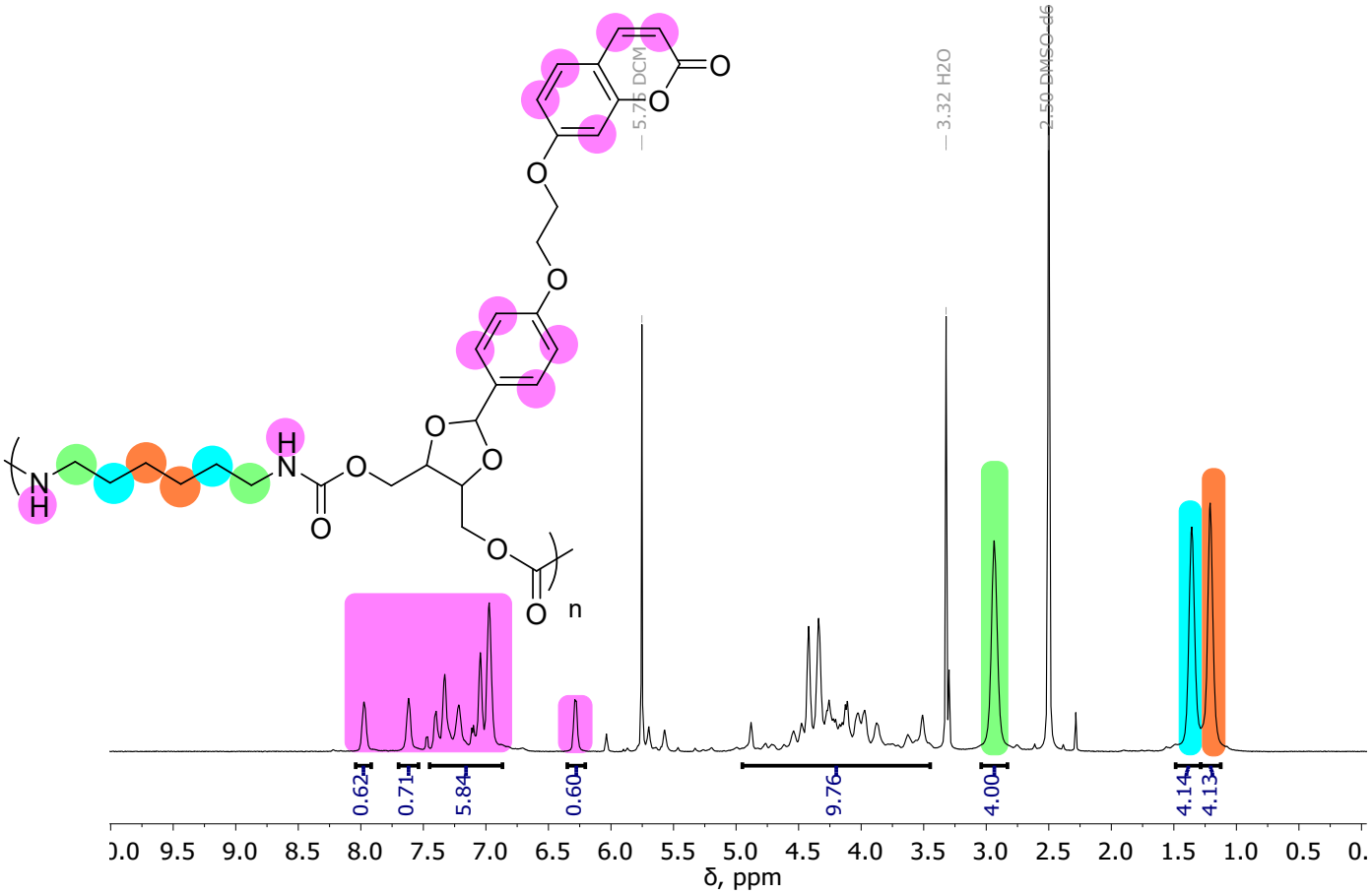

Figure S13. ^{1}H NMR spectrum of **PHU$_1$-Coum** in DMSO-d$_6$.

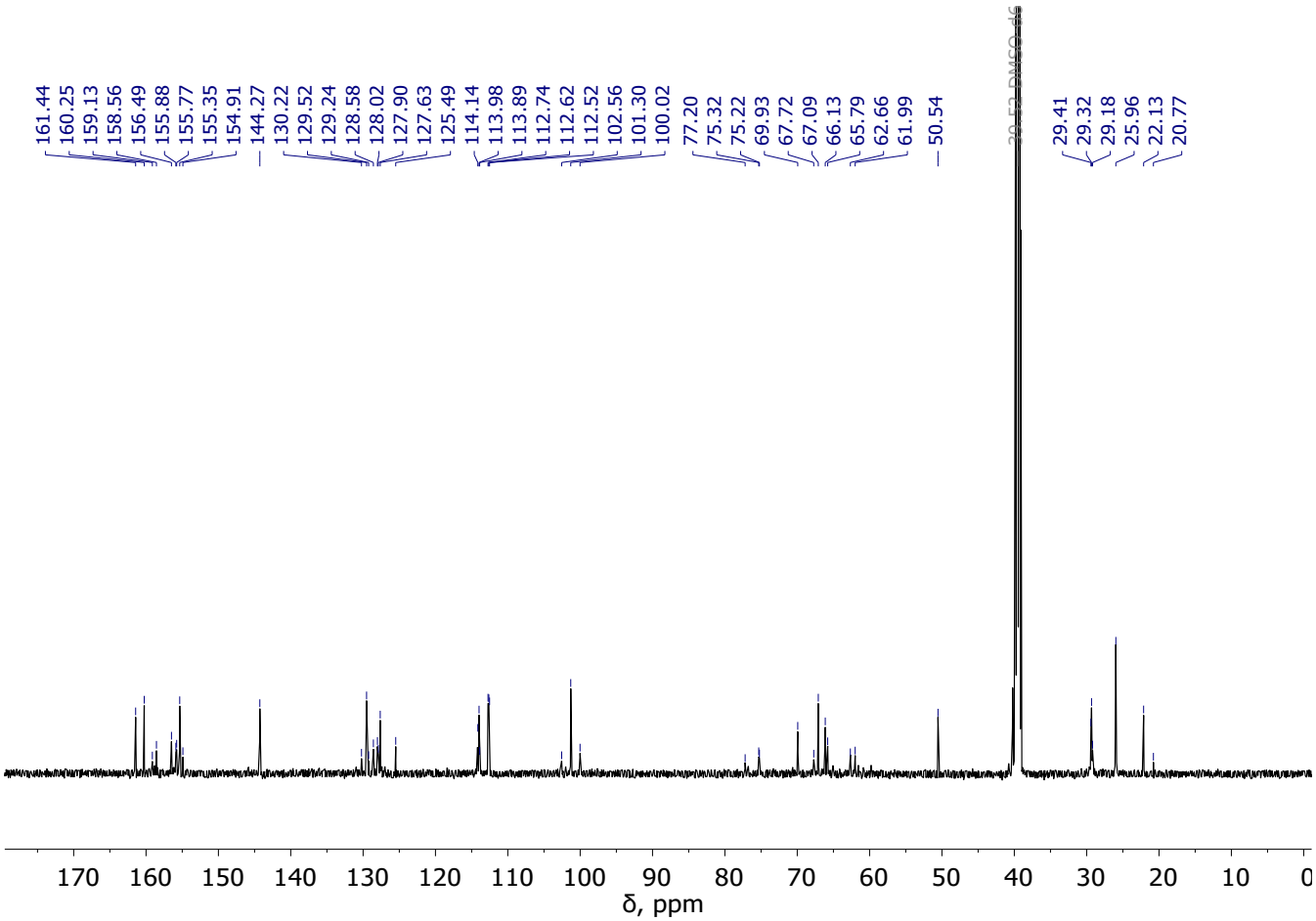

Figure S14. ^{13}C NMR spectrum of **PHU$_1$-Coum** in DMSO-d$_6$.

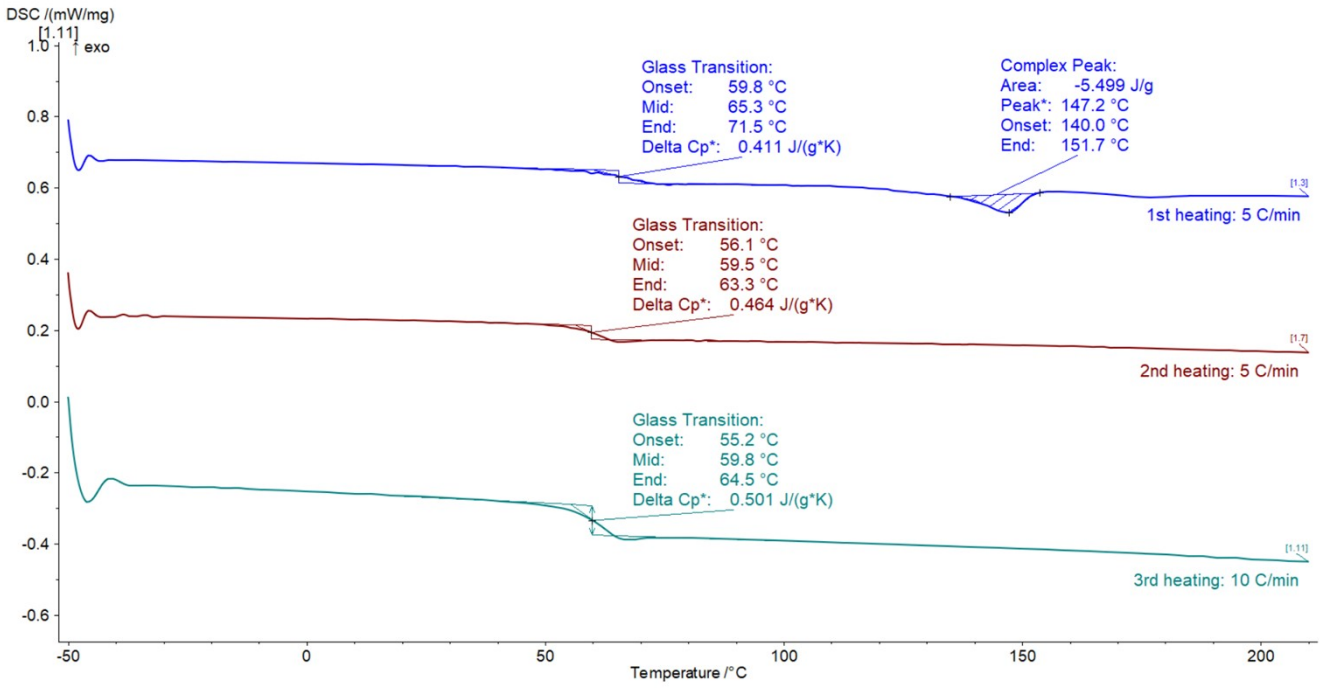

Figure S15. DSC plot of **PHU$_1$-Coum**.

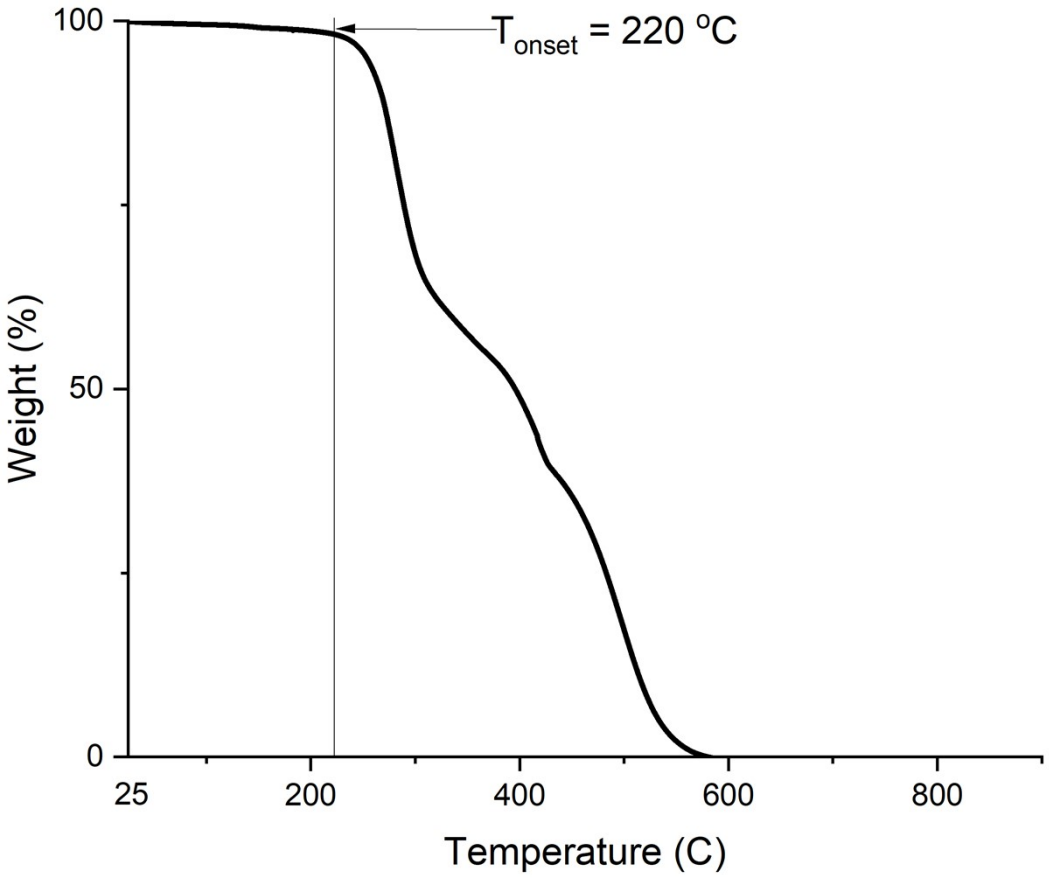

Figure S16. TGA plot of **PHU_1-Coum**.

The Mw/Mn ratios of the synthesized PHUs ranged from 6.4 to 12.9, depending on the fluorescent aldehyde structure employed (Table 1 and Figure S17). The dispersity (Đ) exceeded the value of 2.0 predicted by Flory's theory for ideal step-growth polymerization.

However, it should be emphasized that Flory's prediction relies on two fundamental assumptions: (i) equal reactivity of functional groups and (ii) independence of reactivity from molecular weight. In the present case, deviation from this prediction can be readily rationalized by considering both assumptions. The system initially consists of solid erythritol dicarbonate (EDC) and solid hexamethylene diamine (HMDA). The reaction is carried out via reactive extrusion at 100 °C, essentially under bulk conditions, with the addition of a polar aprotic solvent, N-methyl-2-pyrrolidone (NMP, 30 wt%), acting as both a hydrogen-bond disruptor and a solvating agent. At the outset, the system is not fully homogeneous. Upon heating, HMDA (T_m = 42 °C) melts and, together with NMP, forms a homogeneous phase. In contrast, EDC has a much higher melting point (T_m = 172.1 °C), well above the reaction temperature, resulting in its non-uniform incorporation into the reaction medium. Moreover, as polymerization proceeds and PHU chains form, the concentration of hydroxyl groups increases substantially. This is expected to significantly affect the solvation environment, dielectric constant, and hydrogen-bonding interactions between monomers and growing chains. These evolving conditions directly violate the assumption of constant reactivity throughout the course of polymerization. Collectively, these factors provide a clear physicochemical basis for PHU_1 deviations from Flory's predicted dispersity of 2.

Furthermore, in the subsequent step, the PHU modification with fluorescent aldehydes is carried out in solution. As the degree of modification reaches 60–80%, this may further influence the observed polymer dispersity as well as its interactions with the GPC column. Lastly, the yields of the modification reaction for **PHU_1-Flu** and **PHU_1-Coum** are 62 and 50 wt%, respectively. Consequently, partial removal of low-molar-mass oligomers, particularly in the case of **PHU1-Coum**, may occur during purification, leading to a lower dispersity compared to **PHU1-Flu** (Table 1, main text).

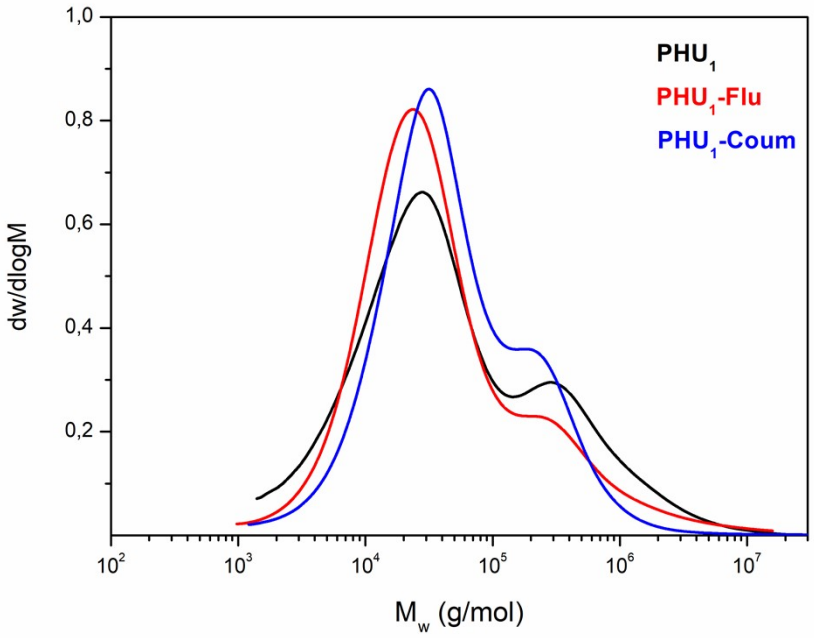

Figure S17. GPC traces of **PHU_1**, **PHU_1-Flu** and **PHU_1-Coum** in 0.1 M $Li(CF_3SO_2)_2N$ (LiTFSI) solution in DMF at 50 °C.

V. Photophysical properties of modified PHU polymers

V.1. Photophysical properties

Figure S18 highlights the distinct photophysical behavior of PHU polymers in solution and in the solid state in the form of thin film, as evidenced by both absorption and emission spectra. The most pronounced difference is observed in the Stokes shift, which is significantly larger for thin films compared to dilute solutions. In addition, the solid-state spectra exhibit broader absorption and emission bands, attributable to intermolecular interactions and the formation of aggregated species that are absent or negligible under dilute-solution conditions.

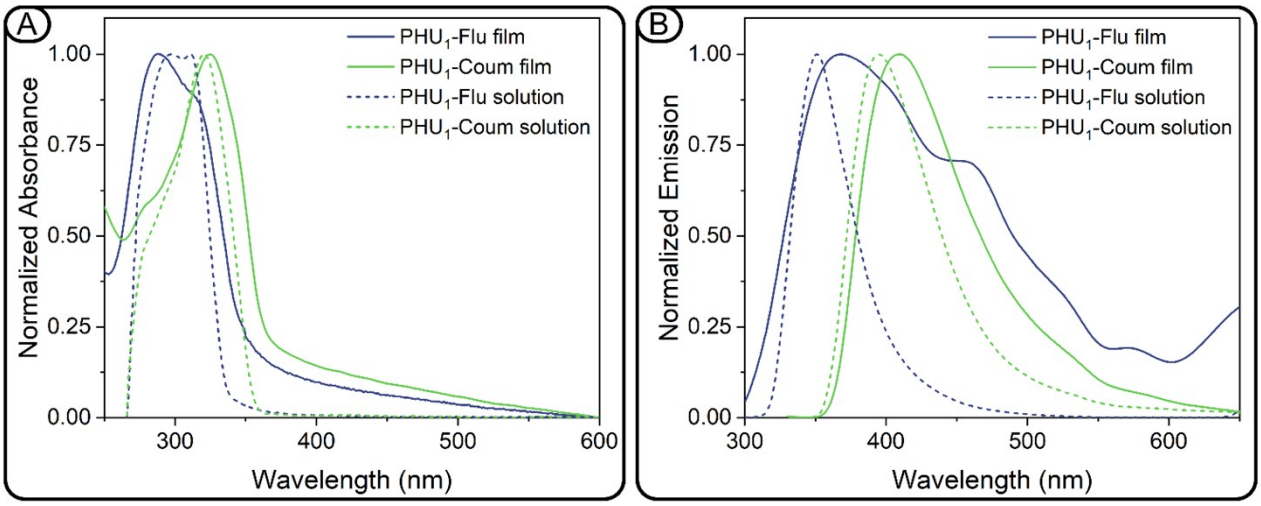

Figure S18. Normalized absorption (**A**) and emission (**B**) spectra of PHU polymers in solution and in thin-film form.

For comparison purposes, the fluorophores A_1 and A_2 were also physically dispersed in a conventional PMMA matrix, widely employed in LSC fabrication. The concentrations of A_1 and A_2 in the PMMA films were adjusted to match those of the corresponding fluorophores incorporated into **PHU$_1$-Flu** and **PHU$_1$-Coum**. PMMA films were prepared from THF solutions using the same spin-coating parameters employed for the PHU-based systems (900 rpm, 60 s), yielding films with comparable thicknesses.

Time-resolved fluorescence and photoluminescence quantum yield (PLQY) measurements were performed on the PHU polymers using dilute DMF solutions. The emission decay profiles were fitted using a tri-exponential model, from which the average fluorescence lifetime (τ) was calculated as the mean averages according to **Equation S3**[S9]:

$$\tau = \frac{\sum_i A_i t_i^{\,2}}{\sum_i A_i t_i} \qquad \text{(S3)}$$

where A_i and t_i are the 3-exponential fit parameters.

As shown in **Table S1**, the covalently functionalized PHU systems exhibit significantly improved solid-state emission properties compared to the corresponding fluorophores physically dispersed in PMMA. In particular, **PHU$_1$-Flu** and **PHU$_1$-Coum** show PLQY values of 58% and 34%, respectively, whereas the corresponding PMMA-based systems exhibit considerably lower values (9.3% for **PMMA+A$_1$** and 8.1% for **PMMA+A$_2$**). These results indicate that covalent incorporation within the PHU backbone partially mitigates aggregation-related quenching and unfavorable intermolecular interactions.

In the fluorene-based systems, both **PHU$_1$-Flu** and **PMMA+A$_1$** exhibit an additional long-wavelength emission component around 500 nm, commonly attributed to fluorenone-type keto defects reported for fluorene-containing materials. However, the contribution of this component is significantly reduced in the **PHU$_1$-Flu** system, suggesting a more controlled chromophore environment upon covalent incorporation. In the case of the coumarin-

based systems, **PHU$_1$-Coum** also exhibits improved emission efficiency compared to **PMMA+A$_2$**, likely due to the reduced mobility and enhanced stabilization of the fluorophore within the covalently functionalized polymer matrix. A full comparison of the fluorescence lifetime decays is provided in Figures S19 and S20.

Table S1. Photophysical properties of the PHU polymers and of the corresponding dyes physically dispersed in PMMA, analyzed from 5 wt% in DMF (for PHUs) and in THF (for dyes dispersed in PMMA) accordingly: fluorescence maximum positions (λ_{em}^{max}); Photoluminescence Quantum Yield (PLQY); Average fluorescence lifetime decay (τ).

	λ_{em}^{max} **(nm)**	**PLQY [c] (%)**	τ **[d] (ns)**
PHU$_1$-Flu	417, 500	58	0.34 (λ_{em}=417nm); 2.42 (λ_{em}=500nm)
PMMA + A$_1$	350, 490	9.3	0.12(λ_{em}=350nm); 5.08(λ_{em}=500nm)
PHU$_1$-Coum	400	34	0.32 (λ_{em}=400 nm)
PMMA + A$_2$	383	8.1	0.63 (λ_{em}=400 nm)

[a] λ_{ex}=330 nm; [b] λ_{ex}=300 nm

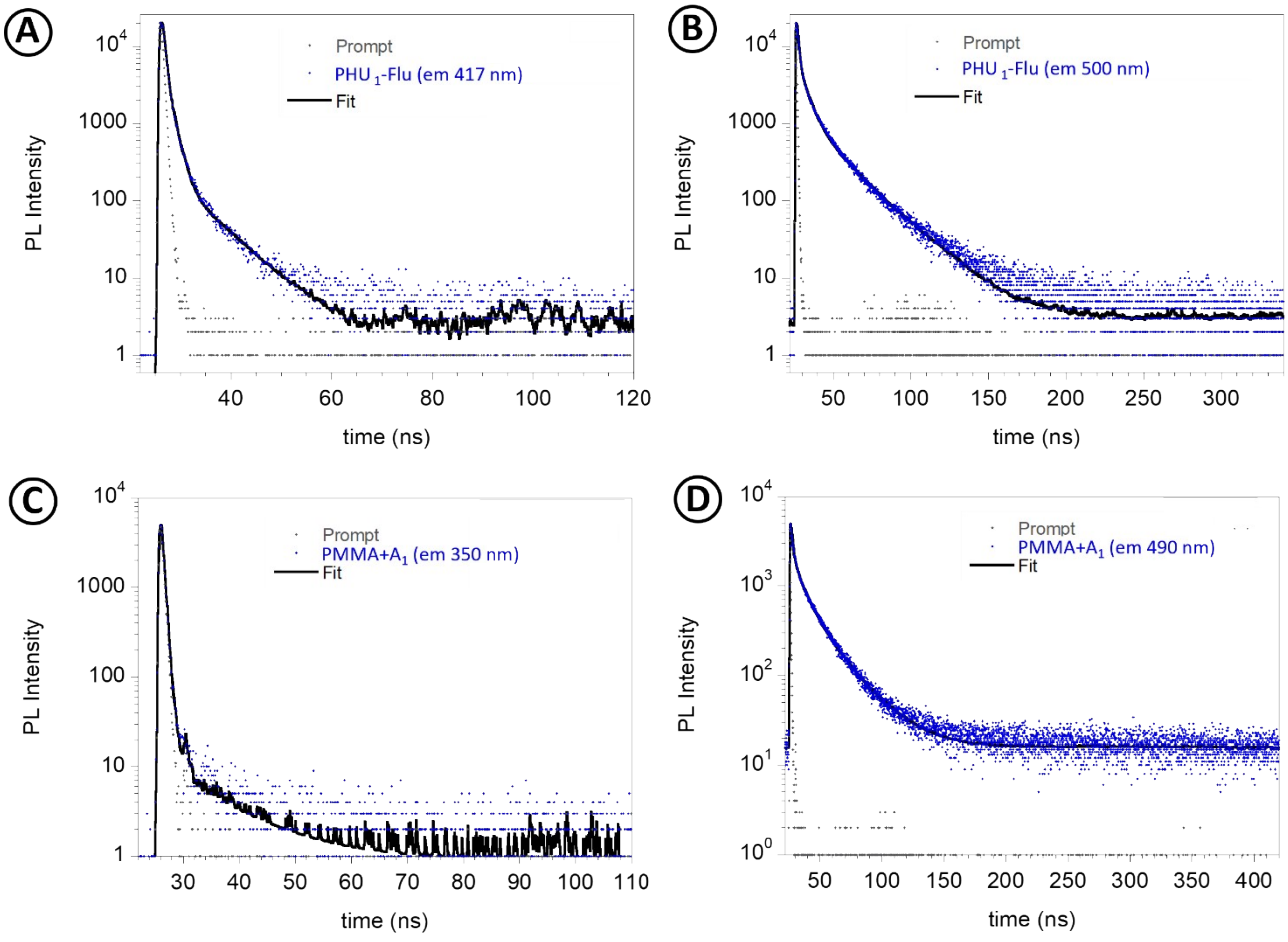

Figure S19. Fluorescence lifetime decay of (A) **PHU$_1$-Flu** as cast film (emission 417 nm); (B) **PHU$_1$-Flu** as cast film (emission 500 nm); (C) A$_1$ physically dispersed in PMMA as cast film (emission 350 nm); (D) A$_1$ physically dispersed in PMMA as cast film (emission 490 nm).

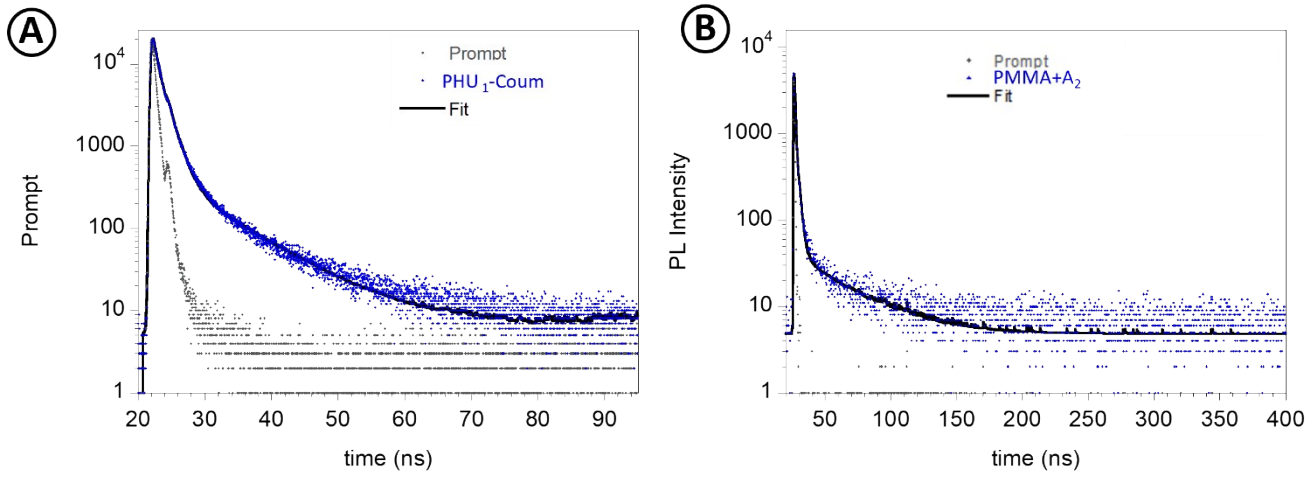

Figure S20. Fluorescence lifetime decay of (A) PHU_1-Coum film; (B) A_2 physically dispersed in PMMA as cast film.

V.2. Photostability study

To evaluate the photostability of modified fluorescent PHU systems and of the corresponding host-guest PMMA-based reference films, continuous irradiation experiments were performed on the thin films using a calibrated solar simulator (AM 1.5G, 100 mW cm^{-2}). The samples were exposed for up to 108 h and analysed at regular time intervals by UV–Vis absorption and photoluminescence (PL) spectroscopy. The evolution of the optical properties of **PHU1-Flu** and **PHU1-Coum** under prolonged irradiation is shown in Figure S21.

For **PHU1-Flu**, the UV-Vis absorption spectra remain largely unchanged over time, indicating good stability of the ground-state absorption properties (Figure S21A). However, a slight decrease in emission intensity is observed upon prolonged irradiation (Figure S21B), accompanied by the emergence of a weak green-band emission around 500 nm. This behaviour is consistent with previously reported photodegradation pathways of fluorene-based systems.[S12-S13]

In the case of **PHU_1-Coum**, a slight reduction in the absorption band at ~325 nm is observed over time (Figure S21C), which may be associated with coumarin photoreactions, such as [2+2] cycloaddition (photodimerization), as reported in the literature.[S14-S16] However, no significant changes in the emission profile (Figure S21D) are observed, but only a moderate decrease in emission intensity (~27% after 108 h), suggesting that such processes remain limited under the present conditions. Coumarin photodimerization is known to occur under UV irradiation (λ > 320-350 nm); however, under the broad-spectrum AM 1.5G irradiation employed here, combined with the restricted segmental mobility of the glassy polymer matrix, the extent of these photoreactions is expected to remain limited. Importantly, no visible yellowing or loss of transparency was observed for either system after prolonged irradiation, and both films remained optically clear.

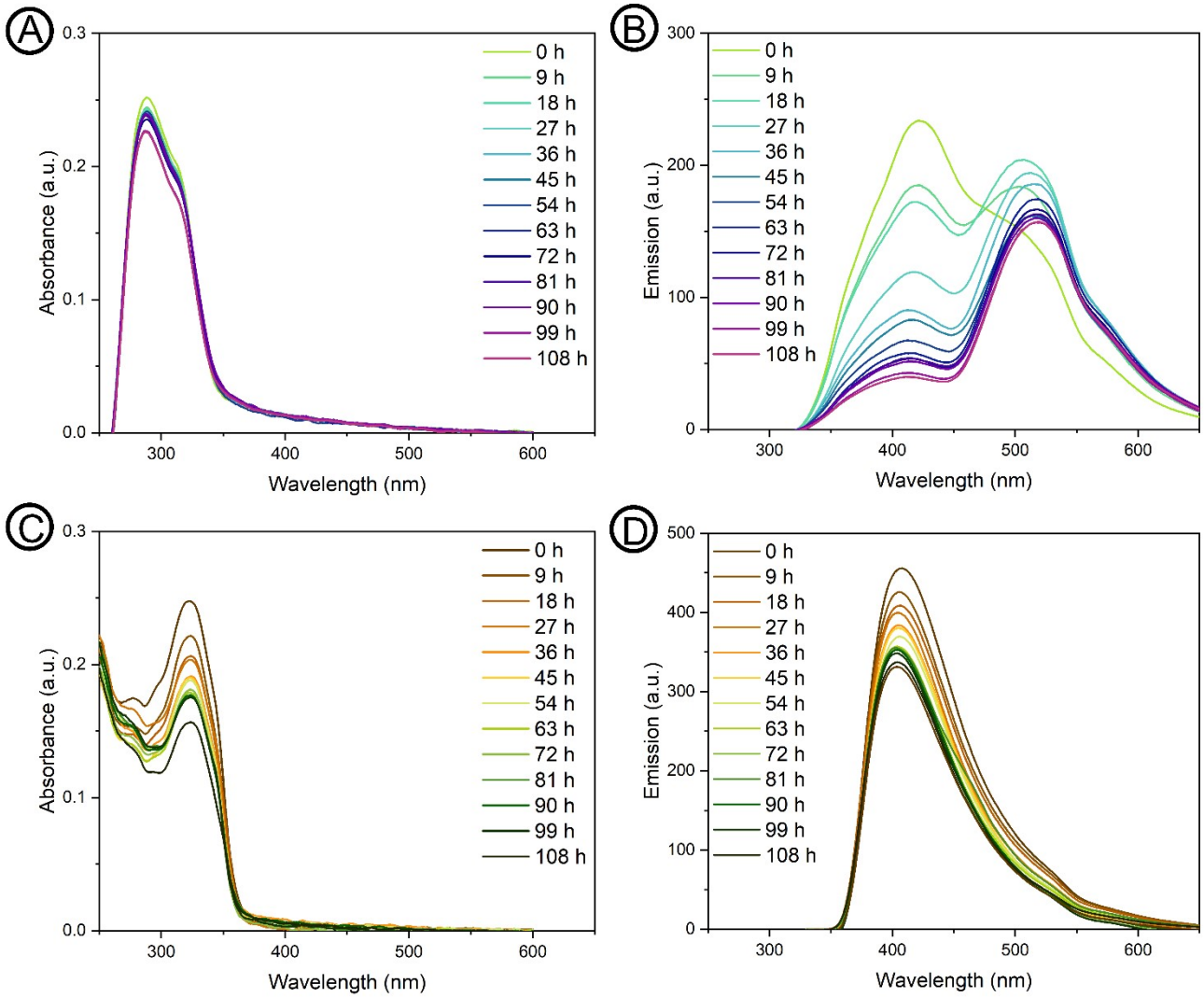

Figure S21. Photostability assessment under continuous solar simulator irradiation (AM 1.5G, 100 mW cm^{-2}): UV-Vis absorption spectra and photoluminescence emission of PHU1-Flu (A, B) and PHU1-Coum (C, D) polymers, measured at different irradiation times.

For comparison, the host-guest PMMA-based systems were also analysed under identical irradiation conditions (Figure S22). In the case of **PMMA+A_1**, the emission profile is dominated by a broad low-energy band centred around ~500 nm, while the higher-energy fluorene emission is significantly suppressed. This behaviour is consistent with the formation of fluorenone-type keto defects,[S12-S13] which are commonly reported in fluorene-based materials under photooxidative conditions. Such defect states act as efficient low-energy emissive traps, promoting energy-transfer processes and accelerating non-radiative decay pathways. The stronger contribution of the ~500 nm emission in **PMMA+A_1** compared to **PHU_1-Flu** suggests that physically dispersed fluorophores experience increased intermolecular interactions and local aggregation within the PMMA matrix, facilitating degradation and defect formation during irradiation. In contrast, the covalent incorporation of the fluorophores within the PHU backbone partially restricts chromophore mobility and mitigates these processes, preserving the primary fluorene emission over time.

Similarly, **PMMA+A_2** exhibits a significantly faster decrease in PL intensity than **PHU_1-Coum** (Figures S22D and S23). This behaviour likely originates from the higher mobility of the physically dispersed coumarin derivatives within the PMMA matrix, which facilitates intermolecular interactions and photoinduced deactivation pathways. In contrast, the covalently functionalized PHU system shows a slower decrease in normalized emission intensity toward a plateau value (Figure S23), indicating improved stabilization of the fluorophore within the polymer environment.

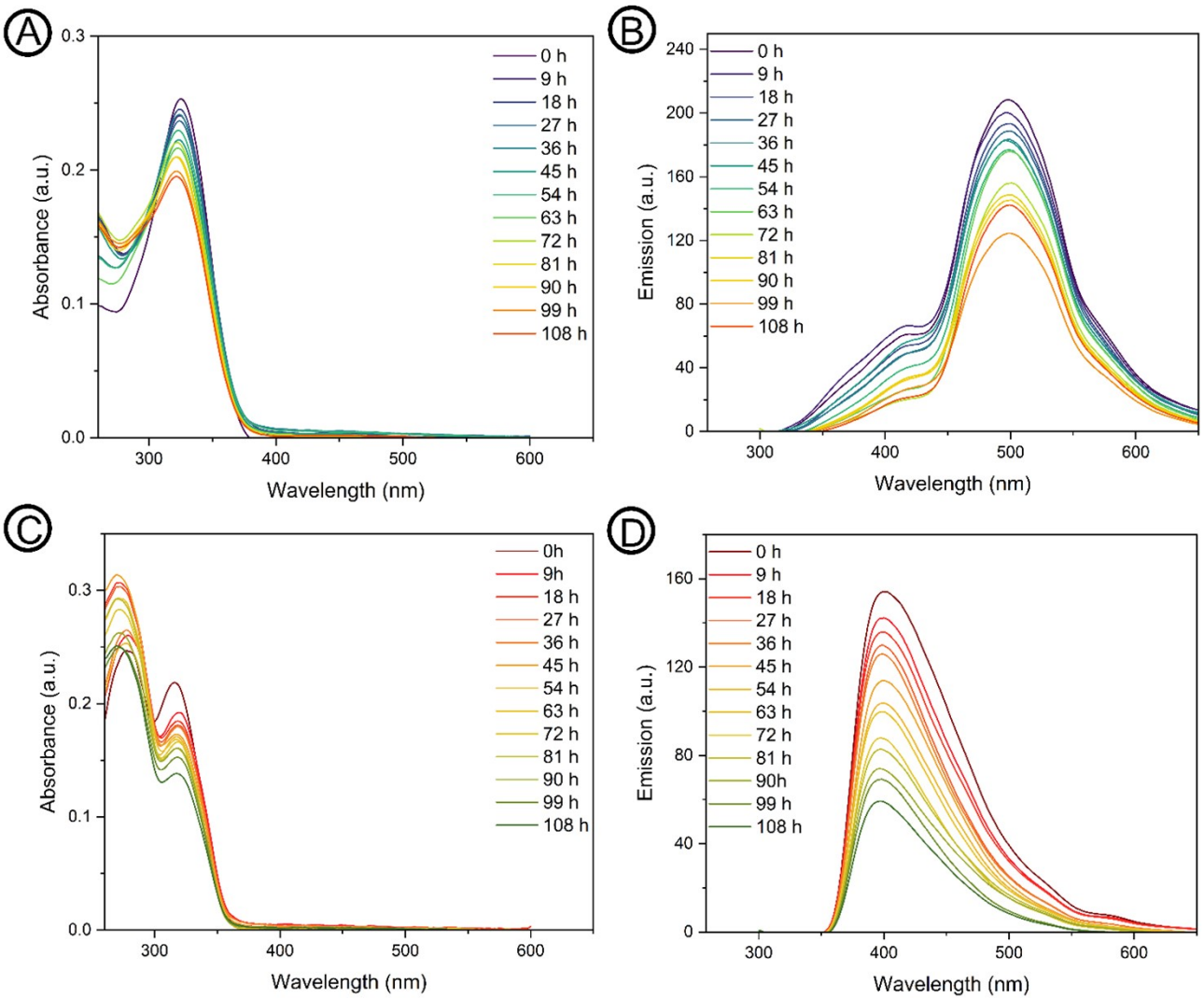

Figure S22. Photostability assessment under continuous solar simulator irradiation (AM 1.5G, 100 mW cm^{-2}): UV-Vis absorption spectra and photoluminescence emission of **PMMA+A_1** (A, B) and **PMMA + A_2** (C, D) systems, measured at different irradiation times.

The normalized PL intensity evolution under continuous irradiation (Figure S23) demonstrates that the PHU-based systems exhibit improved photostability compared to the corresponding PMMA-based films, supporting the beneficial role of covalent incorporation in limiting fluorophore degradation and aggregation-related quenching processes.

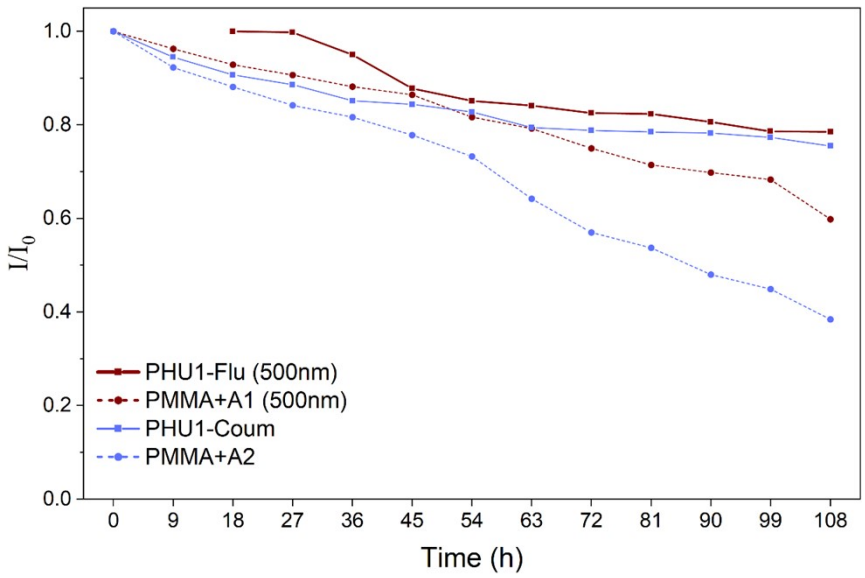

Figure S23. Evolution of the normalized photoluminescence intensity (I/I_0) under continuous AM 1.5G irradiation for PHU-based and PMMA-based systems. For PHU1-Flu and PMMA+A1 systems, the emission intensity of the band peaking at 500 nm was monitored.

VI. Optical and Photovoltaic Characterization of thin-film modified PHU-based devices

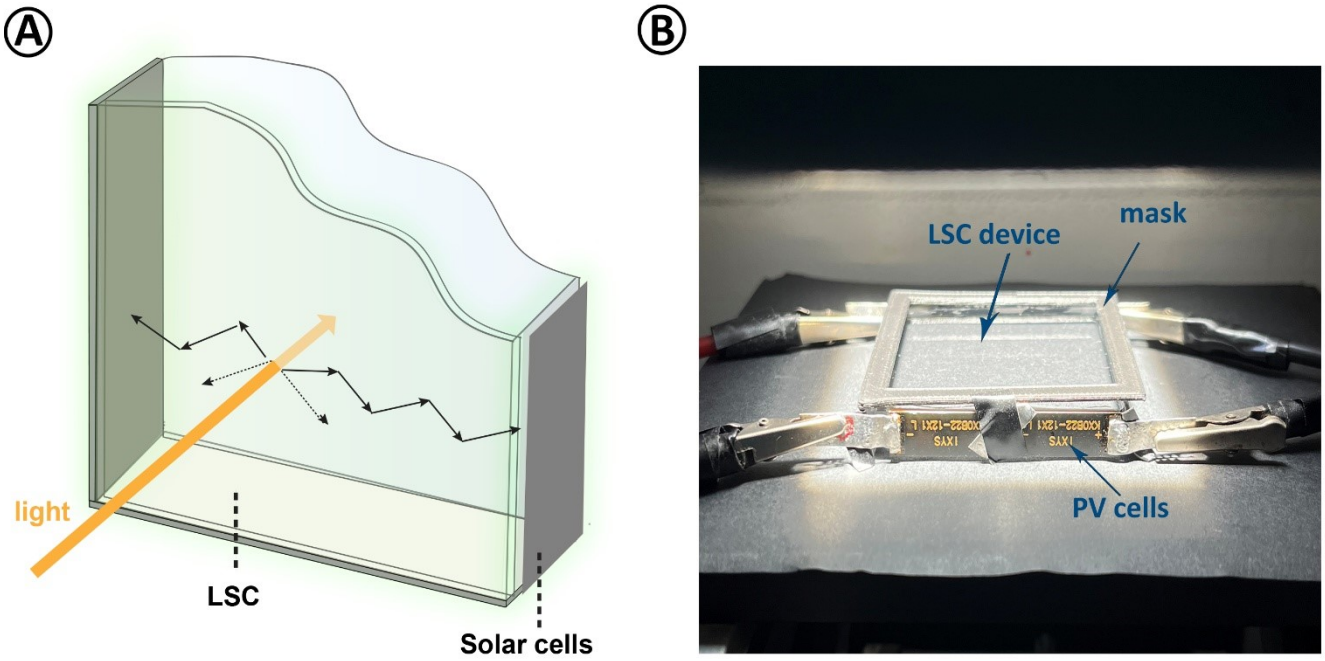

Figure S24. (A) Schematic illustration of the LSC device architecture, showing light absorption by the luminescent medium, waveguiding within the slab, and photon collection at the edges by attached solar cells. (B) Photograph of the **PHU$_1$-Flu** LSC-PV device with silicon solar cells mounted at the edges, measured under a solar simulator operating at AM 1.5 G illumination with an irradiance of 100 mW cm^{-2}.

VI.1. Radiative Overlap (RO)

To better assess the influence and magnitude of reabsorption losses on the performance of the LSC devices, the radiative overlap (RO) was calculated according to **Equation S4**[S17]:

$$RO = \frac{\int Em(\lambda)A(\lambda)d\lambda}{\int Em(\lambda)d\lambda} \cdot 100 \qquad \text{(S4)}$$

where $Em(\lambda)$ is the emission spectrum and $A(\lambda)$ is the absorption spectrum, both obtained from UV-vis spectroscopic measurements.

The calculated RO values are summarized in **Table S2**. Radiative overlap provides a quantitative measure of the spectral overlap between absorption and emission (**Figure S18**); therefore, minimizing reabsorption losses requires this parameter to be as low as possible, ideally approaching zero ($RO \rightarrow 0$).

Table S2. Radiative Overlap (RO) of PHU-based LSC devices.

LSC devices	RO (%)
PHU$_1$-Flu	13.68
PHU$_1$-Coum	6.77

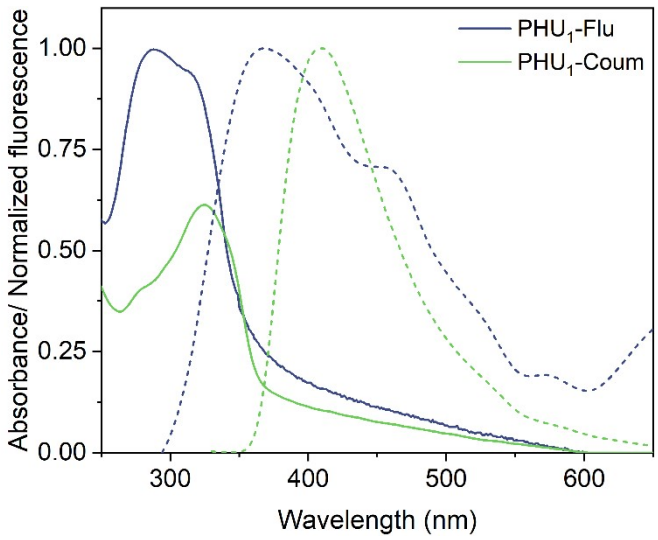

Figure S25. Absorption (1-T(λ)) and normalized emission of PHU-based LSC devices.

VI.2. Photonic Characterization of PHU-based LSC devices

The optical performance of LSCs as photonic systems was assessed by calculating the external photon efficiency (η_{ext}), the internal photon efficiency (η_{int}), and the absorption efficiency (η_{abs}) using the following equations[S18]:

$$\eta_{ext} = \frac{N_{ph-out}}{N_{ph-in}} = \frac{\sum_{i=1300}^{4} \int^{750} P_{i(out)}(\lambda) \frac{\lambda}{hc} d\lambda}{\sum_{i=1300}^{4} \int^{750} P_{(in)}(\lambda) \frac{\lambda}{hc} d\lambda} \quad \text{(S5)}$$

$$\eta_{int} = \frac{N_{ph-out}}{N_{ph-abs}} = \frac{\sum_{i=1300}^{4} \int^{750} P_{i(out)}(\lambda) \frac{\lambda}{hc} d\lambda}{\sum_{i=1300}^{4} \int^{750} P_{(in)}(\lambda) \frac{\lambda}{hc} (1 - 10^{-A(\lambda)}) d\lambda} \quad \text{(S6)}$$

$$\eta_{abs} = \frac{\int_0^{\infty} S_{SO}(\lambda) \left[1 - 10^{-A(\lambda)}\right] d\lambda}{\int_0^{\infty} S_{SO}(\lambda) d\lambda} \quad \text{(S7)}$$

where $N_{ph\text{-}out}$ is the total number of edge-emitted photons summed over four edges (i = 1-4) of the LSC, $N_{ph\text{-}abs}$ is the total number of photons absorbed by the LSC, and $N_{ph\text{-}in}$ is the total number of photons incident on the top surface of the LSC. Also, h is Planck's constant (in J s) and c is the speed of light (in m s^{-1}). $N_{ph\text{-}out}$ is obtained from the sum of the output power spectra, $P_{i(out)}(\lambda)$, measured for each edge of the LSC (in W $nm^{-}1$), where λ is the wavelength of light (in nm). $P_{in}(\lambda)$ is the input power spectrum from the solar simulator incident on the top surface of the LSC (in W nm^{-1}). S_{SO} instead is the source emission spectrum and A is the absorbance, both as a function of wavelength (λ).

All four-edges optical efficiencies for the LSC systems were measured in the 300-750 nm wavelength range under 1000 $W \cdot m^{-2}$ AM1.5G solar simulated light. The results are displayed in **Table S3**. The external (η_{ext}) and internal (η_{int}) photon efficiencies of the host-guest PMMA-based reference systems were measured and compared with those of the corresponding PHU-based devices.

Table S3. Photonic efficiencies of PHU-based and host-guest PMMA-based LSCs.

LSC devices	η_{ext} (%)	η_{int} (%)	η_{abs} (%)
PHU_1-Flu	2.187 ± 0.135	37.271 ± 2.296	8.163 ± 0.408
PHU_1-Coum	1.663 ± 0.041	28.370 ± 0.700	8.090 ± 0.405
PMMA + A1	1.55% ± 0.142	7.62% ± 1.105	12.27 ± 0.118
PMMA + A2	1.23% ± 0.051	6.65% ± 0.809	11.91% ± 0.102

The covalently functionalized PHU systems exhibit consistently higher efficiency values compared to the corresponding host-guest PMMA-based films, indicating reduced non-radiative losses and more efficient emission processes in the solid state.

VI.3. Photovoltaic characterization of PHU-based LSC-PV assemblies

To ensure a comprehensive evaluation of the photovoltaic (PV) response, LSC-PV assemblies were fabricated and tested in a series configuration. Specifically, PV modules, each composed of two monocrystalline silicon cells electrically connected in series and soldered together, were coupled to two opposite edges of the LSC device using a hot-melt adhesive, while the remaining two edges were masked with black tape. Electrical measurements were performed in series using a digital multimeter under simulated AM1.5G solar irradiation at an intensity of 1000 $W \cdot m^{-2}$. The detailed photovoltaic parameters are summarized in **Table S4**.

Table S4. PV parameters and efficiencies of PHU-based LSC-PV assemblies.

LSC devices	Voc (V)	Isc (mA)	FF	η_{dev} (%)	η_{opt} (%)
PHU_1-Flu	2.279 ± 0.009	5.633 ± 0.010	0.657 ± 0.004	0.337 ± 0.003	2.048 ± 0.018
PHU_1-Coum	2.257 ± 0.003	5.101 ± 0.018	0.646 ± 0.004	0.298 ± 0.001	1.841± 0.007

The power conversion efficiency (η_{dev}) is defined as the ratio between the electrical power effectively extracted from the PV cells coupled with the LSC edges, and the optical input power hitting the top surface of the LSC. The η_{dev} was further calculated using **Equation S8**[S19]:

$$\eta_{dev} = \frac{V_{OC} \cdot I_{SC} \cdot FF}{P_{opt}^{in} A_{LSC}} \quad \text{(S8)}$$

where FF, I_{SC} and V_{OC} are the fill factor, short-circuit current, and open-circuit voltage of the LSC device, respectively; P_{opt}^{in} is the incident solar power density (mW cm^{-2}) and A_{LSC} is the front illuminated area of the LSC device (cm^2).

The optical efficiency (η_{opt}), provides an estimate of the ability of the LSC to collect and concentrate incident light and was calculated according to **Equation S9**:

$$\eta_{opt} = \frac{I_{SC}}{I_{SC,PV} \cdot G} \quad \text{(S9)}$$

where I_{SC} is the short-circuit current measured when the PV device is coupled to the LSC, $I_{SC,PV}$ is the short-circuit current of the bare PV device under direct solar irradiation, and G is the geometric gain. Considering a total active PV cell area of 4.8 cm^2 and an LSC top surface area of 25 cm^2, the geometric gain was calculated to be 5.21.

VI.4. Average Visible-light Transmissivity (AVT) and Light Utilization Efficiency (LUE) of PHU-based LSC systems

Additional considerations were made by evaluating two figures of merit related to the transparent nature of the devices. The average visible transmittance (AVT) quantifies the optical transparency of the LSCs as perceived by the human eye under photopic conditions and was defined according to **Equation S10**[S20]:

$$AVT\% = \frac{\int T\%(\lambda) \cdot V(\lambda) \cdot S(\lambda)\, d\lambda}{\int V(\lambda) \cdot S(\lambda) d\lambda} \quad \text{(S10)}$$

where $T\%(\lambda)$ is the wavelength-dependent transmissivity of the device measured by UV-vis spectroscopy, $V(\lambda)$ represents the photopic response of the human eye to light, and $S(\lambda)$ corresponds to the AM1.5G solar spectrum expressed as photon flux ($cm^{-2}\ s^{-1}$).

The Light Utilization Efficiency (LUE) provides a more appropriate metric for comparing different devices in terms of their potential application as transparent photovoltaic systems. It is defined as the product of the AVT and η_{dev} of the LSC devices, as expressed in **Equation S11**[S20]:

$$LUE = AVT \cdot \eta_{dev} \quad \text{(S11)}$$

The results of the two figures of merit are reported in **Table S5** below.

Table S5. Average Visible Transmission (AVT) and Light Utilization Efficiency (LUE) of PHU-based LSC systems.

LSC devices	AVT (%)	LUE (%)
PHU_1-Flu	89.62	0.30
PHU_1-Coum	87.23	0.26

For comparative purposes, Table S6 summarizes literature-reported performance metrics of representative colorless and semi-transparent LSCs. The analysis is deliberately limited to systems employing luminophores with absorption bands located outside the visible region, specifically in the UV or NIR spectral ranges, in order to preserve optical transparency within the visible range. When the original publications did not report a complete set of relevant performance parameters, the corresponding entries are indicated as "n/a", and no values were extrapolated or estimated in the absence of primary data. The table compiles reported values of AVT, LUE, η_{ext}, η_{int}, and η_{dev}, together with the year of publication and the active material, in accordance with the unified reporting frameworks proposed by Yang *et al.* and Debije *et al.* [S18-S19]

Table S6: Comparison of key performance parameters (η_{ext}, η_{int}, η_{dev}, AVT, LUE) for recent colorless luminescent solar concentrators (LSCs).

	Colorless LSCs	AVT (%)	LUE (%)	η_{ext} (%)	η_{int} (%)	η_{dev} (%)	Year	Ref.
1	Luminescent PHUs	90	0.30	2.19	37.27	0.34[a]	2026	**This work**
2	Anthracene AIEgens	99	n/a	<3	63	0.5[a]	2026	ref[S21]
3	Polymeric AIEgens	86	0.25	1.64	33	0.29[a]	2025	ref[S22]
4	NIR-bacteriochlorophyll	73-94	n/a	1	n/a	0.04	2025	ref[S23]
5	ZnO QDs	80.3	n/a	n/a	n/a	up to 3.80[a] and 5.45[b]	2024	ref[S24]

6	Mn:CsPbCl3 Mn:CsPbCl3-3/PS	n/a	n/a	n/a	n/a	0.43-0.77[c]	2024	ref[S25]
7	CISSe/ZnS QDs	n/a	n/a	2.28	12.52	0.5[a]	2024	ref[S26]
8	SiQDs	86	n/a	n/a	n/a	0.27[a]	2022	ref[S27]
9	Ultraviolet and Near-Infrared Dual-Band	75	2.6	n/a	n/a	3	2021	ref[S28]
10	CISeS/ZnS QDs	n/a	n/a	n/a	n/a	n/a	2015	ref[S29]
11	NIR-cyanine derivatives	86	n/a	n/a	n/a	0.4	2014	ref[S30]

[a]calculated with mc-Si solar cells, [b]calculated with OPV solar cells, [c]calculated with Perovskite solar cells.

In comparison with the data summarized in Table S6, the PHU-based LSCs demonstrate performance that is comparable to, and in several cases exceeds, that of previously reported transparent and colorless LSC systems.

VII. References

S1 S. V. Zubkevich, M. Makarov, R. Dieden, L. Puchot, V. Berthé, S. Westermann, A. S. Shaplov and D. F. Schmidt, *Macromolecules*, 2024, **57**, 2385–2393.

S2 G. R. Fulmer, A. J. M. Miller, N. H. Sherden, H. E. Gottlieb, A. Nudelman, B. M. Stoltz, J. E. Bercaw and K. I. Goldberg, *Organometallics*, 2010, **29**, 2176–2179.

S3 J. Moreau, U. Giovanella, J. Bombenger, W. Porzio, V. Vohra, L. Spadacini, G. Di Silvestro, L. Barba, G. Arrighetti, S. Destri, M. Pasini, M. Saba, F. Quochi, A. Mura, G. Bongiovanni, M. Fiorini, M. Uslenghi and C. Botta, *ChemPhysChem*, 2009, **10**, 647–653.

S4 L. Li, R. Matsuda, I. Tanaka, H. Sato, P. Kanoo, H. J. Jeon, M. L. Foo, A. Wakamiya, Y. Murata and S. Kitagawa, *J. Am. Chem. Soc.*, 2014, **136**, 7543–7546.

S5 Z. Zhou, Y. Yuan, Y. Xie and M. Li, *Catal. Lett.*, 2018, **148**, 2696–2702.

S6 Q. Xie, J. Li, X. Wen, Y. Huang, Y. Hu, Q. Huang, G. Xu, Y. Xie and Z. Zhou, *Carbohydr. Res.*, 2022, **512**, 108516.

S7 M. J. Brites, C. Santos, S. Nascimento, B. Gigante and M. N. Berberan-Santos, *Tetrahedron Lett.*, 2004, **45**, 6927–6930.

S8 S. Cao, Y. Xia, J. Shao, B. Guo, Y. Dong, I. A. B. Pijpers, Z. Zhong, F. Meng, L. K. E. A. Abdelmohsen, D. S. Williams and J. C. M. Van Hest, *Angew. Chem. Int. Ed.*, 2021, **60**, 17629–17637.

S9 B. Valeur and M. N. Berberan-Santos, *Molecular Fluorescence: Principles and Applications*, Wiley, 1st edn., 2012.

S10 C.-D. Nechifor, D.-O. Dorohoi and C. Ciobanu, .

S11 B. P. Thapliyal and R. Chandra, *Polymer International*, 1991, **24**, 7–13.

S12 M. Liu, X. Shi, L. Li, J. Zhang, Z. Huang, W. Zhang, N. Zhou, Z. Zhang and X. Zhu, *Macromolecular Chemistry and Physics*, 2021, **222**, 2100092.

S13 R. Grisorio, G. Allegretta, P. Mastrorilli and G. P. Suranna, *Macromolecules*, 2011, **44**, 7977–7986.

S14 W. Jivaramonaikul, P. Rashatasakhon and S. Wanichwecharungruang, *Photochem Photobiol Sci*, 2010, **9**, 1120–1125.

S15 C. S. Collins, M. Zhang, C. Sturgill, C. X. Ruff, B. Melton and M. Stefik, *Mater. Adv.*, 2025, **6**, 4881–4892.

S16 C. Salgado, M. P. Arrieta, V. Sessini, L. Peponi, D. López and M. Fernández-García, *Polymer Degradation and Stability*, 2020, **178**, 109204.

S17 L. R. Wilson, B. C. Rowan, N. Robertson, O. Moudam, A. C. Jones and B. S. Richards, *Appl. Opt.*, 2010, **49**, 1651.
S18 M. G. Debije, R. C. Evans and G. Griffini, *Energy Environ. Sci.*, 2021, **14**, 293–301.
S19 C. Yang, H. A. Atwater, M. A. Baldo, D. Baran, C. J. Barile, M. C. Barr, M. Bates, M. G. Bawendi, M. R. Bergren, B. Borhan, C. J. Brabec, S. Brovelli, V. Bulović, P. Ceroni, M. G. Debije, J.-M. Delgado-Sanchez, W.-J. Dong, P. M. Duxbury, R. C. Evans, S. R. Forrest, D. R. Gamelin, N. C. Giebink, X. Gong, G. Griffini, F. Guo, C. K. Herrera, A. W. Y. Ho-Baillie, R. J. Holmes, S.-K. Hong, T. Kirchartz, B. G. Levine, H. Li, Y. Li, D. Liu, M. A. Loi, C. K. Luscombe, N. S. Makarov, F. Mateen, R. Mazzaro, H. McDaniel, M. D. McGehee, F. Meinardi, A. Menéndez-Velázquez, J. Min, D. B. Mitzi, M. Moemeni, J. H. Moon, A. Nattestad, M. K. Nazeeruddin, A. F. Nogueira, U. W. Paetzold, D. L. Patrick, A. Pucci, B. P. Rand, E. Reichmanis, B. S. Richards, J. Roncali, F. Rosei, T. W. Schmidt, F. So, C.-C. Tu, A. Vahdani, W. G. J. H. M. Van Sark, R. Verduzco, A. Vomiero, W. W. H. Wong, K. Wu, H.-L. Yip, X. Zhang, H. Zhao and R. R. Lunt, *Joule*, 2022, **6**, 8–15.
S20 C. J. Traverse, R. Pandey, M. C. Barr and R. R. Lunt, *Nat. Energy*, 2017, **2**, 849–860.
S21 Z. Yang, Y. Peng, Z. Liu, Y. Bai, Q. Jiang, S. Xue, P. Alam, Z. Qiu and B. Zhong Tang, *Advanced Materials*, 2026, e23640.
S22 E. Tatsi, G. R. Ragno, A. Nitti, C. Botta, S. Turri, D. Pasini and G. Griffini, *Commun. Chem.*, 2025, **8**, 312.
S23 S. F. H. Correia, B. P. Falcão, G. Figueiredo, B. M. C. Vaz, L. S. Contieri, L. M. De Souza Mesquita, J. Almeida, J. C. Fradinho, D. C. G. A. Pinto, L. Fu, P. S. André, S. P. M. Ventura, R. A. S. Ferreira and V. Sencadas, *J. Mater. Chem. A*, 2025, **13**, 11886–11898.
S24 M. D. J. Fimbres-Romero, Á. Flores-Pacheco, M. E. Álvarez-Ramos and R. Lopez-Delgado, *ACS Omega*, 2024, **9**, 28008–28017.
S25 S. Oh, S. W. Bae, T. H. Kim, G. Kang, H. Jung, Y.-H. Kim and M. Park, *J. Mater. Chem. A*, 2024, **12**, 33193–33202.
S26 Y. Chen, F. Ge, Y. Lai, L. Wang, X. Zhao, R. Wang, S. Peng, X.-J. Wu and Y. Zhou, *ACS Appl. Mater. Interfaces*, 2024, **16**, 14072–14081.
S27 S. Han, J. Wen, Z. Cheng, G. Chen, S. Jin, C. Shou, H.-C. Kuo and C.-C. Tu, *Opt. Express*, 2022, **30**, 26896.
S28 C. Yang, W. Sheng, M. Moemeni, M. Bates, C. K. Herrera, B. Borhan and R. R. Lunt, *Adv. Energy Mater.*, 2021, **11**, 2003581.
S29 F. Meinardi, H. McDaniel, F. Carulli, A. Colombo, K. A. Velizhanin, N. S. Makarov, R. Simonutti, V. I. Klimov and S. Brovelli, *Nature Nanotech*, 2015, **10**, 878–885.
S30 Y. Zhao, G. A. Meek, B. G. Levine and R. R. Lunt, *Advanced Optical Materials*, 2014, **2**, 606–611.